



Oscillon formation from preheating in asymmetric inflationary potentials

Rafid Mahbub 

*Department of Physics, Gustavus Adolphus College, Saint Peter, MN 56082, USA**

Swagat S. Mishra 

Center for Astronomy and Particle Theory,

School of Physics and Astronomy,

University of Nottingham, Nottingham, NG7 2RD, UK†

Abstract

We investigate the possibility of oscillon formation during the preheating phase of asymmetric inflationary potentials. We analytically establish the existence of oscillon-like solutions for the Klein-Gordon equation for a polynomial potential of the form $V(\phi) = \frac{1}{2}\phi^2 + A\phi^3 + B\phi^4$ using the small amplitude analysis, which naturally arises as a Taylor expansion of the α -attractor E-model for $\phi \ll M_{\text{pl}}$ and $\alpha \sim \mathcal{O}(1)$. We perform a detailed numerical analysis to study the formation of nonlinear structures in the α -attractor E-model using the publicly available lattice simulation code *CosmoLattice* for parameters in the range $10^{-5} \lesssim \alpha \lesssim 5 \times 10^{-4}$. We find the backreaction of the field fluctuations onto the evolution of the homogeneous inflaton condensate to be significant for $\alpha \lesssim 2 \times 10^{-4}$ for which we observe the formation of highly nonlinear structures with average equation of state $w \simeq 0$. These nonlinear structures maybe interpreted as *oscillons*, providing evidence that they can form during the inflaton oscillations around an asymmetric potential and are found to be present for the entirety of the runtime of our simulations, comprising $\gtrsim 40\%$ of the total energy density.

* mahbub@gustavus.edu

† swagat.mishra@nottingham.ac.uk

CONTENTS

I. Introduction	2
II. Small amplitude analysis and existence of oscillon-like cores	5
III. Instability bands of the E-model	10
A. Linear stability analysis and Floquet theory	10
B. Results for the E-model	12
IV. Lattice results	15
A. $\mathcal{CosmoLattice}$ setup and parameters	15
B. Backreaction from inhomogeneous dynamics	17
C. Power spectra and nonlinear structure formation	20
V. Discussion	26
VI. Conclusions	28
VII. Acknowledgments	29
A. Deriving $\mathcal{CosmoLattice}$ parameters from inflationary observables	30
B. Physical sizes of overdensities	31
References	31

I. INTRODUCTION

Cosmic inflation is at present the leading paradigm that explains the origin of structure in the Universe through vacuum quantum fluctuations during such a period of accelerated expansion of space [1–6]. Through the temperature anisotropies of the Cosmic Microwave Background (CMB), we can place constraints on inflationary observables n_s and r that help us rule in favor and against various inflationary models [7–9]. Inflation ends shortly after the inflaton leaves the slow-roll regime, after which it decays into the particles of the Standard Model via reheating. Originally, reheating was studied as a perturbative process where the inflaton particles decay into other particles independently, thermalizing the Universe and triggering the onset of the Hot Big Bang [10–13]. However,

this perturbative picture ignores collective phenomena that can arise from large and coherent oscillations of the inflaton about the minimum of the potential. For example, Bose condensation effects greatly enhance the rate of the inflaton quanta decay that cannot be captured by perturbative calculations. Of particular importance is the phenomenon of *parametric resonance* (along with *tachyonic resonance*) through which perturbations of the inflaton field and other species can become amplified, leading to copious particle production [14] – with the field fluctuations growing as $\delta\phi_{\mathbf{k}} \propto e^{\mu_{\mathbf{k}}t}$ and $n_{\mathbf{k}} \propto e^{2\mu_{\mathbf{k}}t}$ with a characteristic exponent $\mu_{\mathbf{k}}$ to be defined later. Description of these phenomena requires a non-perturbative treatment. Such a non-thermal period of particle production precedes the usual thermal reheating phase and has been aptly named *preheating* [10, 15, 16]. The period of preheating gives rise to very interesting nonlinear phenomena that are of great interest to cosmologists.

Generic non-linear scalar field theories can exhibit localized configurations in space which oscillate with time. Such configurations can be obtained in scalar field theories with potentials that open up away from (are shallower than) a quadratic minimum $\frac{m^2\phi^2}{2}$ such that the inflaton feels the effects of attractive self-interaction as it oscillates about the minimum. Such localized and dense configurations are called *oscillons* [17–21]. These soliton-like phenomena were first observed in granular and dissipative media [22, 23], which subsequently found their place in the study of preheating in inflationary dynamics. Initial studies on oscillons in cosmology were performed in the context of cosmological phase transitions [24–26]. In more recent times, oscillons have been linked to seeding primordial black holes [27–30] and primordial gravitational waves [31–37] among other interesting phenomena. More recently still, oscillons have found their way into the realm of dark matter, in particular ultra-light dark matter (ULDM). Since oscillons do not have a conserved charge associated with them, they are not technically stable (they decay through the emission of radiation [38–41]). Nevertheless, since these quasi-stable objects can be extremely long-lived and, combined with the fact that they can be produced in large-enough abundances relevant to cosmology, they can be used to model the formation of non-linear structure in ULDM [42–45].

Since oscillon formation requires potentials that are shallower than a quadratic potential around the minimum, there are various inflationary models that can be used as a prototype for their formation. Oscillon formation has been studied in ϕ^6 theories, both analytically and numerically in Refs. [46–48], where it was shown that their field configuration acquires a flat-top feature around the central regions of the core. Moreover, it has also been studied in axion monodromy potentials in Refs. [49–52], hilltop potentials in Refs. [53, 54] and in the α -attractor T-model in Refs. [55, 56]. In Ref. [55], the

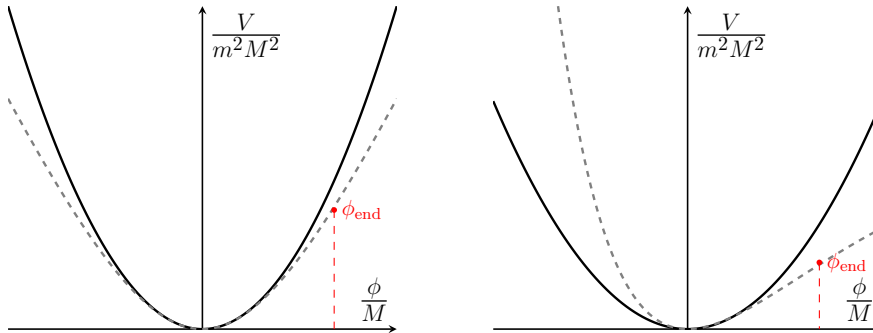


FIG. 1. Illustrations of symmetric (left panel) and asymmetric (right panel) potentials near a quadratic minimum where ϕ_{end} indicates the field value where inflation ends and preheating (presumably) begins. While a shallow symmetric potential opens up on both sides of $\phi = 0$, the asymmetric potential does so only for $\phi > 0$. Hence, the inflaton feels attractive self-interaction at only one side of the potential during the oscillations.

authors used the T-model to quantify the differences between $n = 1$ and $n > 1$ (where the minima are quadratic and non-quadratic respectively at leading order), leading to quite different field configurations as end products. They showed that oscillons can form when $n = 1$ such that the time-averaged equation of state parameter $\langle w \rangle \rightarrow 0$. In cases where $n > 1$, initially dense transients form which fragment into radiation after a few e -folds with $\langle w \rangle \rightarrow \frac{1}{3}$. However, the question of whether oscillons can form in asymmetric potentials has not been addressed adequately in the existing literature. Unlike their symmetric counterparts, asymmetric potentials usually do not open up away from the quadratic minimum on both sides. Hence, the question of whether oscillons do form in such potentials becomes important since the oscillating inflaton might only be experiencing the attractive self-interaction on one side of the minimum.¹ These differences between symmetric and asymmetric potentials are illustrated in Fig. (1). Moreover, since there are only a few well-known asymmetric inflationary potentials (*e.g.* the Starobinsky model), performing a comprehensive study into the matter becomes difficult due to the limited number of asymmetric potentials available. However, see Refs. [33, 35] for previous studies on oscillon formation in asymmetric potentials in the context of production of gravitational waves.

In this paper, we examine the possibility of oscillon formation (or, more generally, nonlinear structure formation) in the α -attractor E-model [61, 62] using detailed 3d nu-

¹ Even in the absence of self-interactions, nonlinear structures can form due to the amplification of metric perturbations that are coupled to the inflaton fluctuations. For example, the scalar perturbations of the simplest ϕ^2 theory (without any self-interaction) undergo parametric resonant amplification on time scales that are much longer than the oscillon formation time scale in the interacting theory [57–60].

merical lattice simulations. It is divided into the following sections: in Sec. II, we show that oscillon-like solutions can exist in a generic asymmetric polynomial potential of the form $V(\phi) = \frac{1}{2}\phi^2 + A\phi^3 + B\phi^4$ using the method of small amplitude analysis in $(1+1)$ - d . A potential of this form arises from the small amplitude limit of the E-model α -attractor [62]. In Sec. III, Floquet analysis is used to generate the instability chart for inflaton perturbations during the preheating phase which can be used to demonstrate the existence of a broad-band resonance region followed by multiple narrow ones. In Sec. IV we carry out $3d$ lattice simulations of the E-model potential and confirm the formation of nonlinear structures, which can be interpreted as oscillons. By performing a volume integral of the overdensities above a certain threshold, we demonstrate that oscillons can be copiously produced, constituting over 40% of the total energy, for values of α in the relevant range. Finally, in Sec. V the consequences of the smallness of α is discussed – particularly in relation to the predicted levels of tensor perturbations and the running of the scalar spectral tilt. There we also comment on the effects of long-term gravitational clustering and some simulation specific issues.

In this work, we adopt the mostly negative convention for the Friedmann-Lemaître-Robertson-Walker (FLRW) metric such that $ds^2 = dt^2 - a^2(t)\delta_{ij}dx^i dx^j$, ignoring the effects of metric perturbations. We also use natural units where $c = \hbar = 1$ and the reduced Planck mass is denoted as $(8\pi G)^{-1} = M_{\text{pl}}^2$ which has a numerical value of 2.44×10^{18} GeV.

II. SMALL AMPLITUDE ANALYSIS AND EXISTENCE OF OSCILLON-LIKE CORES

Even though oscillons are nonlinear structures and should be studied in full generality using non-perturbative techniques and numerical simulations, a great deal of information about them can be obtained by using the *small amplitude analysis* [38, 46–48, 63–65]. More importantly, we can use this technique to confirm whether or not a given scalar potential can admit solutions where the field configurations exhibit oscillon-like cores, which correspond to solutions of the nonlinear Klein-Gordon equation with centrally peaked profile oscillating in time. However, since the small amplitude analysis relies upon an expansion in the powers of the scalar field, it is only limited to cases where the amplitude of the scalar field oscillations is much smaller compared to some mass scale (usually the Planck scale M_{pl}). Moreover, oscillons relevant in the field of cosmology are usually ones with large amplitude. Hence, the small amplitude analysis should only serve as a first step at ascertaining their existence.

We consider the α -attractor E-model potential with $n = 1$ [61, 62]. For $n > 2$, the leading order behavior of the minimum ceases to be quadratic. The E-model potential can be written as

$$V(\phi) = V_0 \left[1 - \exp \left(-\lambda(\alpha) \frac{\phi}{M_{\text{pl}}} \right) \right]^2 \quad (\text{II.1})$$

where $\lambda(\alpha) = \sqrt{2/3\alpha}$. Since Eq. (II.1) is an asymmetric potential, we can Taylor expand it around the minimum to derive a polynomial potential that will be easier to study with the small amplitude analysis. Expanding it up to $\mathcal{O}(\phi^4)$, we have

$$U(\phi) \equiv \frac{V(\phi)}{m^2 M_{\text{pl}}^2} \approx \frac{1}{2} \left(\frac{\phi}{M_{\text{pl}}} \right)^2 - \underbrace{\frac{\lambda}{2} \left(\frac{\phi}{M_{\text{pl}}} \right)^3}_{\text{asymmetric}} + \frac{7\lambda^2}{24} \left(\frac{\phi}{M_{\text{pl}}} \right)^4 \quad (\text{II.2})$$

Considering a $(3+1)$ -d FLRW metric of the form $ds^2 = dt^2 - a^2(t)\delta_{ij}dx^i dx^j$, we have the following action

$$S = \int d^4x \sqrt{-g} \left[\frac{M_{\text{pl}}^2}{2} R + \frac{1}{2} \partial_\mu \phi \partial^\mu \phi - V(\phi) \right] \quad (\text{II.3})$$

where $\sqrt{-g}$ is the metric determinant and R is the Ricci scalar. The following scalings are performed which transform the variables (t, x, ϕ) into dimensionless quantities: $\tilde{t} = mt$, $\tilde{x} = mx$ and $\tilde{\phi} = \phi/M_{\text{pl}}$. With these redefinitions, and restricting ourselves to $(1+1)$ -d in a non-expanding universe, the following equation of motion can be derived

$$\partial_{\tilde{t}}^2 \tilde{\phi} - \partial_{\tilde{x}}^2 \tilde{\phi} + \partial_{\tilde{\phi}} U = 0 \quad (\text{II.4})$$

Equation (II.4) can be solved order-by-order using a perturbative expansion of $\tilde{\phi}$ and frequency ω in terms of an expansion parameter ε . To that end, these variables can be written down as

$$\tilde{\phi} = \sum_{n=1}^{\infty} \varepsilon^n \tilde{\phi}_{(n)} \quad (\text{II.5})$$

$$\omega^2(\varepsilon) = 1 + \sum_{n=1}^{\infty} \varepsilon^n \omega_{(n)} \quad (\text{II.6})$$

Furthermore, we rescale the (\tilde{t}, \tilde{x}) variables to make them ε -dependent. This is carried out via $y = \varepsilon \tilde{x}$ and $\tau = \omega(\varepsilon) \tilde{t}$. With these, we have the following

$$-\omega^2 \partial_\tau^2 \tilde{\phi} + \varepsilon^2 \partial_y^2 \tilde{\phi} = \tilde{\phi} - \frac{3\lambda}{2} \tilde{\phi}^2 + \frac{7\lambda^2}{6} \tilde{\phi}^3 \quad (\text{II.7})$$

In the following steps, we work up to $\mathcal{O}(\varepsilon^3)$ in the expansion and we will show that the first correction to the frequency ω is obtained precisely at this order. Unlike [47], the

even powers of $\tilde{\phi}$ will not vanish since $\partial_{\tilde{\phi}}U$ contains a $\tilde{\phi}^2$ term. The aim is to be able to express the evolution of each $\tilde{\phi}_{(n)}$ in the form

$$\partial_{\tau}^2 \tilde{\phi}_{(n)} + \tilde{\phi}_{(n)} = \mathcal{F}_{(n)} \left[\tilde{\phi}_{(n-1)}, \partial_{\tau} \tilde{\phi}_{(n-1)}, \partial_{\tilde{\phi}} U(\tilde{\phi}_{(n-1)}) \right] \quad (\text{II.8})$$

where \mathcal{F}_n is a forcing term that is a function of the field variable and its derivatives in the previous order in the expansion. Since at each order n we are seeking a differential equation of the form of a forced harmonic oscillator, we shall assume that the solutions do not have very strong spatial dependence. It is trivial to show that, at $\mathcal{O}(\varepsilon)$, the first order field is a simple harmonic oscillator $\partial_{\tau}^2 \tilde{\phi}_{(1)} + \tilde{\phi}_{(1)} = 0$, with a solution that behaves as $\tilde{\phi}_{(1)}(\tau, y) = f(y) \cos \tau + \mathcal{O}(\varepsilon^2)$.

At $\mathcal{O}(\varepsilon^2)$, we have the following

$$\omega_{(1)} \partial_{\tau}^2 \tilde{\phi}_{(1)} + \partial_{\tau}^2 \tilde{\phi}_{(2)} + \tilde{\phi}_{(2)} - \frac{3\lambda}{2} \tilde{\phi}_{(1)}^2 = 0 \quad (\text{II.9})$$

The term $\partial_{\tau}^2 \tilde{\phi}_{(1)} \sim \cos \tau$ is a resonance term which will produce a term in the solution which grows as τ . Since we are interested in bounded solutions, we set $\omega_{(1)} = 0$. Solving Eq. (II.9) using the initial conditions $\tilde{\phi}_{(2)}(0, y) = \partial_{\tau} \tilde{\phi}_{(2)}(\tau, y)|_{\tau=0} = 0$, we have

$$\tilde{\phi}_{(2)}(\tau, y) = \frac{\lambda}{4} f^2(y) (3 - 2 \cos \tau - \cos 2\tau) \quad (\text{II.10})$$

Similarly, at $\mathcal{O}(\varepsilon^3)$, the evolution of $\tilde{\phi}$ is given by

$$\partial_y^2 \tilde{\phi}_{(1)} - \omega_{(2)} \partial_{\tau}^2 \tilde{\phi}_{(1)} - \partial_{\tau}^2 \tilde{\phi}_{(3)} - \frac{7\lambda^2}{6} \tilde{\phi}_{(1)}^3 + 3\lambda \tilde{\phi}_{(1)} \tilde{\phi}_{(2)} - \tilde{\phi}_{(3)} = 0 \quad (\text{II.11})$$

After simplifying Eq. (II.11), there also turns out to be a resonance term that needs to be set to zero to obtain bounded solutions. This results in

$$\frac{\partial^2 f(y)}{\partial y^2} + \omega_{(2)} f(y) + \lambda^2 f^3(y) = 0 \quad (\text{II.12})$$

To obtain solutions which are localized and decay to zero at spatial infinity, one requires the condition $\omega_{(2)} < 0$. Also, deriving the first integral of motion (conserved energy)² and imposing conditions of localized solutions, we obtain

$$a^2 \equiv \omega_{(2)} = \frac{\lambda^2}{2} f_0^2 \quad (\text{II.13})$$

² The first integral of motion can be shown to be the following

$$E = \frac{1}{2} (\partial_y f)^2 - \frac{a^2}{2} f^2 + \frac{\lambda^2}{4} f^4$$

obtained by multiplying Eq. (II.12) by $\partial_{\tau} \varphi$ and integrating by parts.

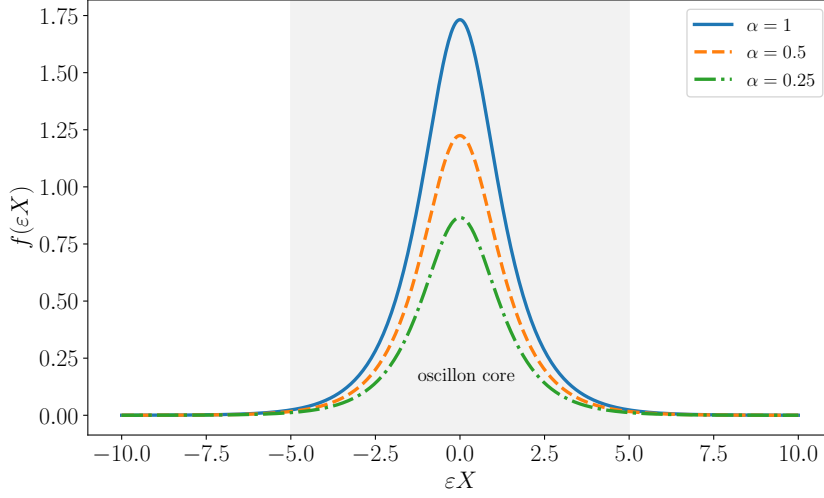


FIG. 2. Oscillon core profile obtained from the 4th-order expansion of the E-model potential for different values of $\lambda(\alpha)$.

Moreover, integration of the conserved energy equation yields the oscillon core profile (shown in Fig. (2))

$$f(y) = \sqrt{2} \frac{a}{\lambda(\alpha)} [1 - \tanh^2(-ay)]^{1/2} = f_0 \operatorname{sech} \left(\frac{f_0}{\sqrt{3\alpha}} y \right) \quad (\text{II.14})$$

Hence, up to $\mathcal{O}(\epsilon^2)$, the solution can be written as

$$\tilde{\phi}_{\text{osc}}(\tau, y) = \epsilon f(y) \cos \tau + \epsilon^2 \frac{\lambda}{4} f^2(y) (3 - 2 \cos \tau - \cos 2\tau) + \mathcal{O}(\epsilon^3) \quad (\text{II.15})$$

with $y = \epsilon \tilde{x}$ and $\tau = \sqrt{1 - \epsilon^2 a^2} \tilde{t}$. Since ϵ is a small expansion parameter, it can be chosen such that $\epsilon \equiv \Phi_0/M_{\text{pl}}$. As a result, we can write

$$\phi_{\text{osc}}(\tau, y) = \Phi(y) \left[\cos \tau + \frac{\lambda}{4} \frac{\Phi(y)}{M_{\text{pl}}} (3 - 2 \cos \tau - \cos 2\tau) \right] + \mathcal{O}(\epsilon^3) \quad (\text{II.16})$$

where $\epsilon M_{\text{pl}} f(y) = \Phi(y)$. Hence, the solution φ_{osc} describes spatially localized profiles which display temporal variations with combinations of the frequency $\omega = \sqrt{1 - \epsilon^2 a^2} m \approx \left(1 - \epsilon^2 \frac{\lambda^2 f_0^2}{4}\right) m$, indicating towards the possibility of oscillon formation in such an asymmetric potential. However, we must remember that this is only an approximation and one needs to verify the existence of such nonlinear objects through lattice simulations which is the goal of the succeeding sections. Furthermore, these calculations only considered one spatial dimension and neglected the effects of expansion. For instance, it can be shown

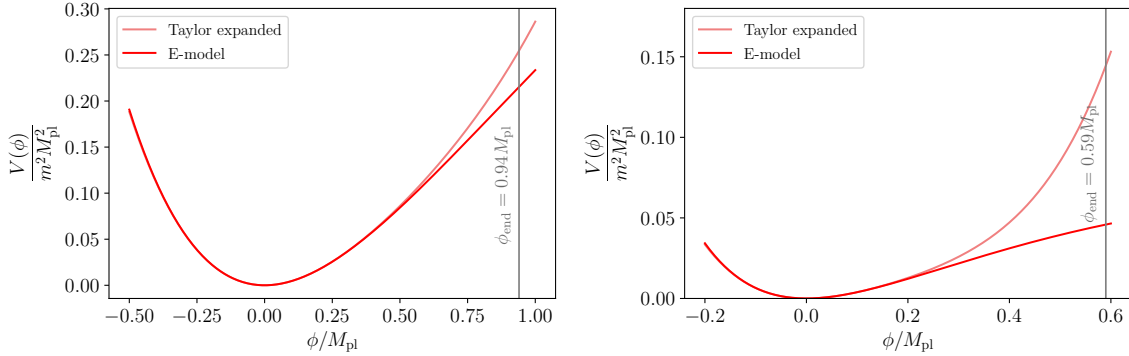


FIG. 3. Comparisons of the E-model and 4th-order polynomial potentials for $\alpha = 1$ (left panel) and 0.1 (right panel). The gray vertical lines correspond to the field values where inflation ends and, hence, preheating commences. This figure aims to show that the Taylor expansion should really be used to model the E-model potential when $\alpha \sim \mathcal{O}(1)$.

that in $d \geq 2$, the energy associated with the oscillon solution decays due to the presence of a friction term [46]

$$\partial_y E = -\frac{d-1}{y} (\partial_y f)^2 \quad (\text{II.17})$$

We note that for a general potential of the form $V(\phi) = \frac{1}{2}\phi^2 + A\phi^3 + B\phi^4$, solutions admitting an oscillon profile may only appear for a range of values in the parameter space of A and B . One can show that, in general

$$f(y) = \sqrt{\frac{16}{3\Gamma(A, B)}} \text{sech}(y) \quad (\text{II.18})$$

for $a = 1$, such that

$$\Gamma(A, B) = 20A^2 - 8B \quad (\text{II.19})$$

For a real solution for $f(y)$, we require that $\Gamma(A, B) > 0$, which restricts the possible values for A and B . Although we have shown that oscillon-like solutions exist for an asymmetric potential, it does not necessarily mean that the inflaton condensate fragments and forms oscillons during preheating. We further note that Eq. (II.2) does not perfectly capture details of the E-model, especially in relation to its plateau region for $\phi > 0$. If we use the field value at the end of inflation as the initial condition for the preheating stage, it can be observed that the values of the potentials are within agreeable limits when $\alpha \sim \mathcal{O}(1)$ and the difference in the values of $V(\phi)$ increases sharply for lower values of α . This is shown in Fig. (3). In what follows, we perform a detailed $3d$ lattice study on the E-model

in pursuit of oscillon formation. For the reasons stated above, we will not use the Taylor expanded potential in the lattice simulations.

III. INSTABILITY BANDS OF THE E-MODEL

Parametric resonance plays a crucial role in governing the growth of perturbations during inflationary preheating [15, 16]. As a result, it is important to identify the existence of instability bands in the parameter space of comoving modes k and the field amplitude and to study the trajectory of modes as they pass through the instability bands due to their time evolution. A linear stability analysis of inflaton perturbations $\delta\phi_{\mathbf{k}}$ can be performed using Floquet theory. In the next subsections, Floquet theory is introduced and applied to the E-model to identify the instability bands of the model.

A. Linear stability analysis and Floquet theory

Before applying Floquet theory, we can study the inflaton fluctuations at the linear order in perturbation theory and search for instability bands. This analysis can be carried out with or without the inclusion of metric perturbations. Specializing to the case where metric perturbations are absent, we consider the inflaton Klein-Gordon equation $\ddot{\phi} + 3H\dot{\phi} - \frac{\nabla^2}{a^2}\phi + \partial_\phi V = 0$ and linearize it around scalar fluctuations $\phi(t, \mathbf{x}) = \phi(t) + \delta\phi(t, \mathbf{x})$, obtaining the following equation for the perturbations

$$\delta\ddot{\phi} + 3H\delta\dot{\phi} + \partial_{\phi\phi}V(\phi)\delta\phi - \frac{\nabla^2}{a^2}\delta\phi = 0 \quad (\text{III.1})$$

or, in Fourier space

$$\delta\ddot{\phi}_{\mathbf{k}} + 3H\delta\dot{\phi}_{\mathbf{k}} + \partial_{\phi\phi}V(\phi)\delta\phi_{\mathbf{k}} + \frac{k^2}{a^2}\delta\phi_{\mathbf{k}} = 0 \quad (\text{III.2})$$

with Bunch-Davies vacuum conditions $\delta\phi_{\mathbf{k}} = 1/(a\sqrt{2k})$ and $\delta\dot{\phi}_{\mathbf{k}} = -i(k/a)\delta\phi_{\mathbf{k}}$. If we consider, to leading order, that the minimum of $V(\phi)$ is quadratic, then the inflaton oscillates about it such that $\phi(t) = \phi_0(t)\cos(mt)$. Ignoring cosmic expansion for the moment (for which ϕ_0 becomes time independent) and setting $a = 1$, Eq. (III.2) takes the form of a parametric oscillator³

$$\delta\ddot{\phi}_{\mathbf{k}} + [k^2 + \partial_{\phi\phi}V(\phi(t))]\delta\phi_{\mathbf{k}} = 0 \quad (\text{III.3})$$

³ If we consider that the typical time period of oscillations is much less than the Hubble timescale, *i.e.* $T = 2\pi/\omega \ll H^{-1}$, then the expansion term can be ignored since $\omega_{\mathbf{k}}(t) \gg H(t)$. This is usually true after a few oscillations when $H \propto 1/t$ drops well below the inflaton mass.

with the term $k^2 + \partial_{\phi\phi}V$ serving as the time-dependent frequency $\omega_{\mathbf{k}}^2(t)$. When metric perturbations were included, the mode equation would take the form

$$\delta\ddot{\phi}_{\mathbf{k}} + \omega_{\mathbf{k}}^2(t)\delta\phi_{\mathbf{k}} = \underbrace{4\delta\dot{\phi}_{\mathbf{k}}\dot{\Psi} - 2\Psi\partial_{\phi}V}_{\text{metric perturbations}} \quad (\text{III.4})$$

where Ψ is the Bardeen potential. Second order differential equations of these forms are also known as the *Hill's differential equation* [66–68] and, according to Floquet theorem, they admit solutions of the form

$$\delta\phi_{\mathbf{k}}(t) = e^{\mu_{\mathbf{k}}t}\mathcal{P}_{(+)}(t) + e^{-\mu_{\mathbf{k}}t}\mathcal{P}_{(-)}(t) \quad (\text{III.5})$$

The quantities $\mu_{\mathbf{k}}$ in the exponents are called Floquet exponents and they describe how the modes grow or decay with time. The functions $\mathcal{P}_{(\pm)}(t)$ are periodic functions with the same period of oscillation as the background field. The $\mu_{\mathbf{k}}$ are complex in general and those modes with $\Re(\mu_{\mathbf{k}}) > 0$ correspond to growing solutions.⁴ For purely imaginary exponents, the modes are oscillatory. The utility of Floquet theory lies in the fact that one can map such ‘zones of instability’ in the form of a Floquet chart. Such a chart comprises of bands of instability in the form of broad and narrow resonance bands.

Apart from a few simple cases, the Floquet exponents need to be computed numerically. However, there exists a relatively straightforward approach using which the Floquet exponents can be numerically calculated [15, 16, 57]. We start by expressing Eq. (III.3) as a system of coupled differential equations in matrix form

$$\delta\dot{\Phi}(t) = \mathcal{U}(t)\delta\Phi(t) \quad (\text{III.6})$$

where $\delta\Phi(t) = [\delta\phi_{\mathbf{k}}, \delta\pi_{\mathbf{k}}]^T$ and $\delta\pi_{\mathbf{k}} = \delta\dot{\phi}_{\mathbf{k}}$. The matrix $\mathcal{U}(t)$ is given by

$$\mathcal{U}(t) = \begin{pmatrix} 0 & 1 \\ -k^2 - \partial_{\phi\phi}V & 0 \end{pmatrix} \quad (\text{III.7})$$

Next, the time period T of the oscillation is determined. If the potential is symmetric, this is as simple as performing the integral

$$T(\phi_{\text{in}}) = 2 \int_0^{\phi_{\text{in}}} \frac{d\phi}{\sqrt{2V(\phi_{\text{in}}) - 2V(\phi)}} \equiv 2T_{(1/2)} \quad (\text{III.8})$$

⁴ This can be seen as the result of violation of the adiabatic condition $|\dot{\omega}/\omega^2| < 1$. As a consequence, the perturbations grow as $\delta\phi_{\mathbf{k}} \sim e^{\mu_{\mathbf{k}}t}$ instead of oscillating as $\delta\phi_{\mathbf{k}} \sim e^{\pm i \int \omega_{\mathbf{k}} dt}$.

where $T_{(1/2)}$ is the period of a half oscillation. However, if the potential is asymmetric, as in the present case, the time period cannot be calculated using the expression above. For odd potentials, one can show that T takes the following form

$$T = T^{(+)} + T^{(-)} = \int_0^{\phi_{\text{in}}} \frac{d\phi}{\sqrt{2V(\phi_{\text{in}}) - 2V(\phi)}} + \int_{\phi_{\text{f}}}^0 \frac{d\phi}{\sqrt{2V(\phi_{\text{f}}) - 2V(\phi)}} \quad (\text{III.9})$$

where ϕ_{f} is the amplitude to which the field rises on the $\phi < 0$ side of the potential that can be determined using energy considerations, namely $V(\phi_{\text{f}}) = V(\phi_{\text{in}})$. The time period can also be calculated using the solution of the background evolution. Now, using a set of orthogonal initial conditions $\{\delta\phi_{\mathbf{k}}^{(1)}(0) = 1, \delta\pi_{\mathbf{k}}^{(1)}(0) = 0\}$ and $\{\delta\phi_{\mathbf{k}}^{(2)}(0) = 0, \delta\pi_{\mathbf{k}}^{(2)}(0) = 1\}$, Eq. (III.3) is evolved from $t = 0$ to T . Then, the Floquet exponents are calculated by

$$\Re(\mu_{\mathbf{k}}^{(\pm)}) = \frac{1}{T} \ln \left[\frac{1}{2} (\delta\phi_{\mathbf{k}}^{(1)} + \delta\pi_{\mathbf{k}}^{(2)}) \pm \frac{1}{2} \sqrt{(\delta\phi_{\mathbf{k}}^{(1)} - \delta\pi_{\mathbf{k}}^{(2)})^2 + 4\delta\phi_{\mathbf{k}}^{(2)}\delta\pi_{\mathbf{k}}^{(1)}} \right] \quad (\text{III.10})$$

such that

$$\Re(\mu_{\mathbf{k}}) = \max \left[\Re(\mu_{\mathbf{k}}^{(\pm)}) \right] \quad (\text{III.11})$$

In Eq. (III.10), all the quantities are evaluated at $t = T$. Hence, the calculation of the instability bands for parametric resonance essentially involves evolving these mode functions using orthogonal initial conditions and searching for the existence of $\Re(\mu_{\mathbf{k}}) > 0$. When evaluated for an entire grid of (k, ϕ_{in}) , the instability regions of the parametric oscillator can be mapped out, which typically display banded structures.

B. Results for the E-model

We now consider parametric resonance occurring in the α -attractor E-model. The potential can be written down as follows

$$V(\phi) = \frac{3}{4}\alpha m^2 M_{\text{pl}}^2 \left(1 - e^{-\sqrt{\frac{2}{3\alpha}} \frac{\phi}{M_{\text{pl}}}} \right)^2 \quad (\text{III.12})$$

The overall constant being $V_0 = \frac{3}{4}\alpha m^2 M_{\text{pl}}^2$ reflects the fact that the potential, at leading order, resembles $\frac{m^2 \phi^2}{2}$. Since the background and mode evolution equations can be made dimensionless, the only relevant parameter in the potential is α . It is important to note that inflaton potentials with a plateau generally exhibit tachyonic instability where the effective mass squared m_{eff}^2 becomes negative [69, 70]. This is also true for the E-model

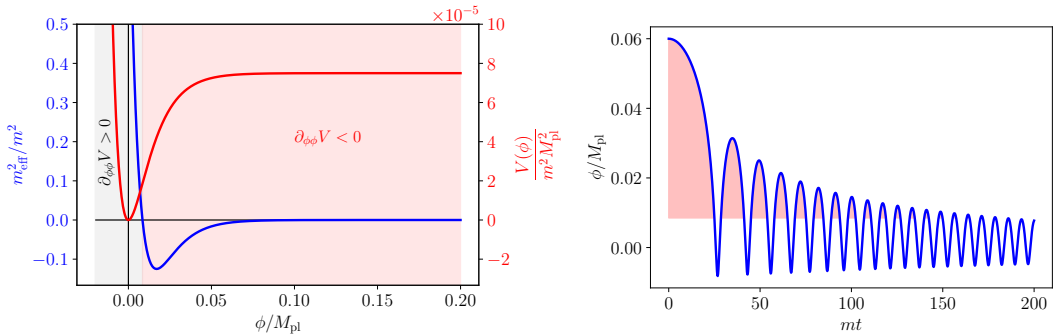


FIG. 4. *Left panel:* The effective mass squared m_{eff}^2 (blue) and the E-model potential (red) are shown for $\alpha = 10^{-4}$. The red shaded region indicates the field values for which $m_{\text{eff}}^2 < 0$. In the plateau region, the effective mass is still negative but asymptotically approaches zero. *Right panel:* The homogeneous background evolution of the field is shown where the red shaded portions indicate the regions where the field oscillations enter the tachyonic instability regimes. As the field amplitude decays due to expansion, the inflaton is unable to access the tachyonic instability regime after a fixed time has passed.

potential which possesses a plateau at large ϕ . For the E-model, it can be shown that $m_{\text{eff}}^2 \equiv \partial_{\phi\phi} V < 0$ when $\phi > \sqrt{\frac{3\alpha}{2}} 0.693 M_{\text{pl}}$. This is shown in Fig. (4). In the left panel we have plots of m_{eff}^2 (solid blue) and $V(\phi)$ (solid red) where we see that $m_{\text{eff}}^2 < 0$ extends throughout the plateau, becoming prominent near the plateau's edge.⁵ The homogeneous field evolution is shown in the right panel. There we observe that during oscillations, ϕ repeatedly enters and exits the tachyonic instability region for a few cycles, before cosmic expansion dampens out the amplitude. A detailed study of tachyonic preheating in plateau inflation can be found in Ref. [71].

In Fig. (5) the variation of the Floquet exponents is shown for two different field values while in Fig. (6), the Floquet charts for the E-model are plotted for $\alpha = 5 \times 10^{-4}$ and 10^{-4} .⁶ They show the existence of a broad instability band for $k \lesssim 0.5m$ and a series of narrower ones for higher values of k . Since the physical wavenumber in an expanding universe is $k/a(t)$, for a given amplitude, the Fourier modes will trace out a path in the instability chart and will pass through one or several of these instability bands.

⁵ The effective mass for the E-model is

$$\frac{m_{\text{eff}}^2}{m^2} = 2e^{-2y} - e^{-y} \quad \text{where} \quad y = \sqrt{\frac{2}{3\alpha}} \phi$$

For asymptotically large field values, $m_{\text{eff}}^2 \simeq -e^{-y} m^2$. Hence the effective mass stays negative throughout, although very nearly zero for large ϕ , until $\phi = \sqrt{\frac{3\alpha}{2}} 0.693 M_{\text{pl}}$.

⁶ For the benefit of the reader, we note that the different $\phi[M_{\text{pl}}]$ in Fig. (5) and (6) refer to the field amplitudes for the $\phi > 0$ excursions of the inflaton. This distinction is necessary due to the asymmetric nature of the E-model potential.

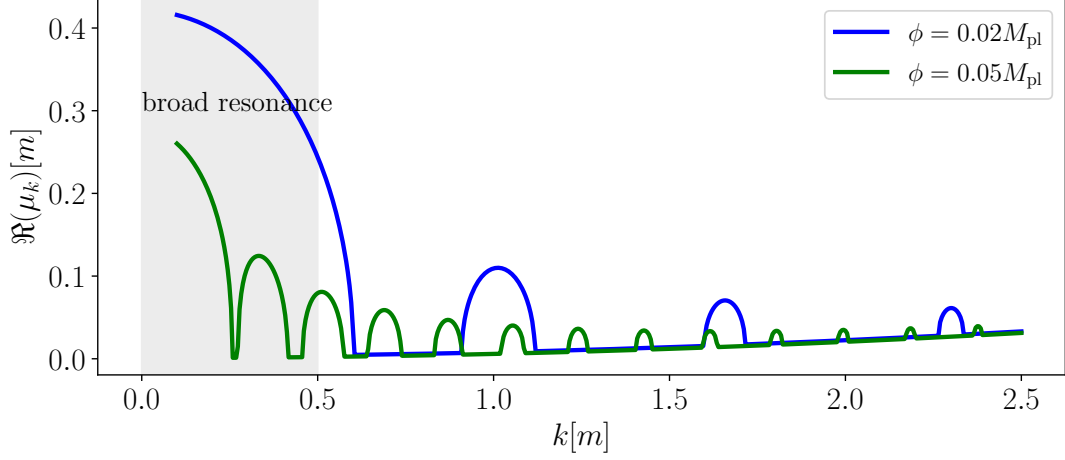


FIG. 5. Variation of the Floquet exponent as a function of k at two different values of the field amplitude. The gray shaded region indicates the broad resonance regime which will be pronounced for $0.02 \lesssim \phi/M_{\text{pl}} \lesssim 0.03$ for $\alpha = 10^{-4}$.

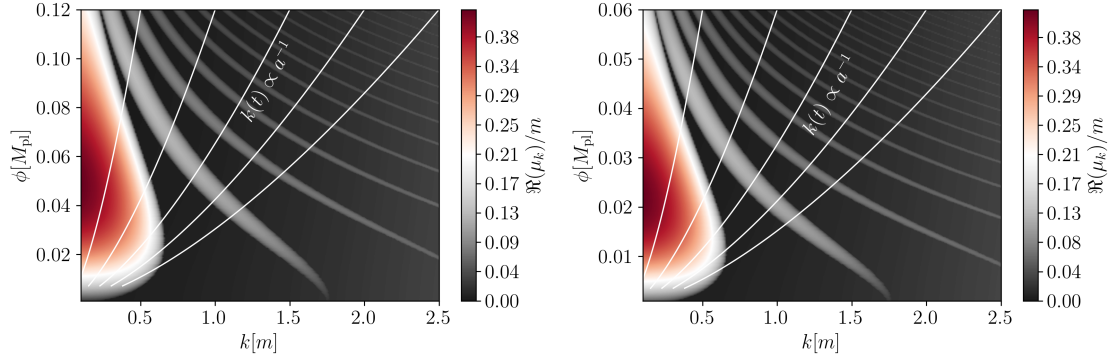


FIG. 6. Floquet charts for the E-model with $\alpha = 5 \times 10^{-4}$ (left panel) and $\alpha = 10^{-4}$ (right panel) with the colorbar denoting the real part of the Floquet exponent $\frac{\Re(\mu_k)}{m}$. The charts show the existence of a broad instability band for $k \lesssim 0.5m$, where $\left[\frac{\Re(\mu_k)}{m}\right]_{\text{max}} \sim 0.40$, and several narrower ones for larger k . The white flow lines show how the physical k -modes pass through different resonance bands as they evolve.

Specifically, if the potential is quadratic near the minimum, one finds $\phi(t) \propto a^{-3/2}(t)\phi_{\text{in}}$ and $k_{\text{phys}}(t) \propto a^{-1}(t)$. For example, a small k -mode can exhibit strong growth as it passes through the broad resonance band as it evolves through time, eventually decreasing as it moves out the band. Likewise, a larger k -mode can initially pass through several of the narrow bands before entering the broad resonance band at late times. The evolution

of the k -modes are shown by the white lines in the instability chart. The crossing of these bands with time can qualitatively explain how the power spectrum $\mathcal{P}_{\delta\phi}(k)$ of the fluctuations should evolve. In particular, one should expect the following

- For comoving modes which are $k \lesssim 0.5m$, there should be a sharp enhancement in $\mathcal{P}_{\delta\phi}(k)$ at relatively early times. We use the word ‘relatively’ to emphasize the fact that the modes do not start out in the broad resonance band at $t = 0$. However, these are the first modes to experience the strong amplification in the perturbations since the k_{phys} corresponding to these comoving modes evolve through to the broad resonance regime the earliest.
- Larger comoving k -modes can experience slight enhancements at early times due to the passage of the corresponding k_{phys} through the narrow resonance bands. At later times, when they enter the broad resonance band, the amplification of these modes will be significantly enhanced and we should expect the peak, which is initially centered at small k , to be shifted to larger k values.

This will be explored in detail in the next section where lattice simulation results are interpreted.

IV. LATTICE RESULTS

Here we present the results of $3d$ lattice simulations on the E-model for different values of α . There are a number of publicly available lattice codes that can be used for studying preheating dynamics – LatticeEasy [72], DEFROST [73], HLattice [74] and PyCool [75] to name a few. We use the publicly available lattice code *CosmoLattice* [76, 77] for our $3d$ simulations. In this section, we first discuss numerical simulation setup and then move on to analyzing the simulation results. Finally, we discuss whether or not the nonlinearities observed from the E-model can be interpreted as oscillons.

A. *CosmoLattice* setup and parameters

Lattice simulations work with dimensionless variables. In terms of the dimensionless variables as $\tilde{t} = mt$, $\tilde{x} = mx$ and $\tilde{\phi} = \frac{\phi}{M_{\text{Pl}}}$, the inhomogeneous inflaton Klein-Gordon equation to be solved takes the form

$$\ddot{\tilde{\phi}} - \frac{\tilde{\nabla}^2}{a^2} \tilde{\phi} + 3 \frac{\dot{a}}{a} \dot{\tilde{\phi}} + \partial_{\tilde{\phi}} \tilde{V} = 0 \quad (\text{IV.1})$$

where the redefined potential now reads

$$\tilde{V}(\tilde{\phi}) = \frac{3}{4}\alpha \left(1 - e^{-\sqrt{\frac{2}{3\alpha}}\tilde{\phi}}\right)^2 \quad (\text{IV.2})$$

In order to consistently solve the preheating dynamics, one must also account for the background expansion of space through the Friedmann and Raychaudhuri equations, given by

$$H^2 \equiv \left(\frac{\dot{a}}{a}\right)^2 = \frac{1}{3M_{\text{pl}}^2} \langle E_{\text{K}} + E_{\text{G}} + E_{\text{V}} \rangle \quad (\text{IV.3})$$

$$\frac{\ddot{a}}{a} = \frac{1}{3M_{\text{pl}}^2} \langle -2E_{\text{K}} + E_{\text{V}} \rangle \quad (\text{IV.4})$$

where E_{K} , E_{G} and E_{V} are the kinetic, gradient and potential energies associated with the inflaton field and $\langle \dots \rangle$ represents spatial averaging. *CosmoLattice*, like most other lattice codes, does not take into account the effects of metric perturbations arising from the Bardeen potential $\Psi(t, \boldsymbol{x})$, because of which we cannot study the nonlinearities arising from gravitational clustering on longer time scales. As previously mentioned, the only free parameter involved in this model is α . The initial field values for the lattice simulations are chosen such that they correspond to the point in field space where inflation ends (ϕ_{end}), which depends on the choice of α . For each value of α , the initial field values are chosen such that constraints on inflationary observables are satisfied – namely the CMB normalization $\mathcal{P}_{\zeta} = 2.1 \times 10^{-9}$ at the pivot scale $k_{\star} = 0.05 \text{ Mpc}^{-1}$, the scalar spectral index $n_s \approx 0.965$ and the scalar-to-tensor ratio $r < 0.036$ [7, 8, 78]. These details are presented in Appendix A.

The numerical simulations are performed for the following parameters and corresponding initial conditions for the homogeneous field

α	$\phi_{\text{in}}[M_{\text{pl}}]$	$\phi_{\text{in}}[\text{GeV}]$
5×10^{-4}	0.109	2.65×10^{17}
10^{-4}	0.058	1.42×10^{17}
10^{-5}	0.023	5.57×10^{16}

TABLE I. The different choices of the parameter α along with the corresponding ϕ_{in} .

Table I summarizes the different choices of α used in the simulations along with the corresponding initial value for the field ϕ_{in} . With an inflationary excursion corresponding

to 55 e -folds since the pivot scale becomes superhorizon, we find that the mass scale for this model is set to $m \approx 1.27 \times 10^{-5} M_{\text{pl}}$, which does not change irrespective of the value of α . The main results of this work were obtained from simulations with lattice size $N = 256^3$ and $\tilde{k}_{\text{IR}} = 0.05$ (here \tilde{k}_{IR} is the minimum infrared cut-off⁷ for the reciprocal lattice) while some results pertaining to longer time evolution, mainly the time evolution of the equation of state (EoS) parameter, were obtained with $N = 128^3$. Moreover, the time integration was carried out using the 2nd-order Velocity-Verlet (VV2) algorithm available in *CosmoLattice*. Higher order VV algorithms can also be used. However, we found no quantitative difference in the outputs of the spatially averaged quantities and, as a result, VV2 is a perfectly reasonable choice for a time integrator in terms of accuracy and speed. We do note that, at least for the E-model, there will be significant numerical differences for lower resolution grids, starting from $N = 64^3$, with the solutions displaying *overshooting* at around $\tilde{t} \sim 50$. Hence, we recommend that the smallest grid size with which the simulations are to be carried out should be $N = 128^3$.

It should also be of interest to analytically check whether fragmentation of the inflaton condensate occurs for the chosen parameters. In Refs. [28, 79, 80], bounds on the parameters of α -attractor T and E-models for inflaton fragmentation were derived. For an asymmetric potential of the form $V(\phi) = \frac{1}{2}m^2\phi^2 - A\phi^3$, it was found that

$$A > \frac{400}{9\sqrt{6}\pi} \left(\frac{m^2}{M_{\text{pl}}} \right) \left(\frac{0.1}{r_A} \right) \approx 5.78 \left(\frac{m^2}{M_{\text{pl}}} \right) \left(\frac{0.1}{r_A} \right) \quad (\text{IV.5})$$

where $r_A \approx 0.1$. This can be used provide bounds on the value of α necessary for fragmentation. One finds that

$$\alpha \lesssim 5 \times 10^{-3} \left(\frac{r_A}{0.1} \right)^2 \quad (\text{IV.6})$$

Hence, according to this analytical estimate, we should be able to observe inflaton fragmentation for all the three parameters listed in Table I.

B. Backreaction from inhomogeneous dynamics

From Eq. (IV.1), we notice that the presence of the $-\tilde{\nabla}^2\tilde{\phi}$ term can play an important role in the time evolution of the volume averaged field. Although not significant during the slow-roll phase of inflation, the inhomogeneities can, nevertheless, become very

⁷ The infrared cut-off is defined as

$$\tilde{k}_{\text{IR}} = \frac{2\pi}{\tilde{L}}$$

where \tilde{L} is comoving length of the cubic lattice. With $\tilde{k}_{\text{IR}} = 0.05$, the cubic lattices have sides of comoving lengths $\tilde{L} = 125.6m^{-1}$.

important during the preheating phase, leading to potentially significant backreactions on the oscillating homogeneous inflaton. Hence, if we scan through the parameter α , we may be able to find a point where $\tilde{\phi}$ loses its oscillatory nature when the gradient term kicks in, indicating the onset of backreaction from growing perturbations. In Ref. [55], it was found that backreaction is significant in α -attractor models for $M \ll M_{\text{pl}}$, which in the present case corresponds to $\alpha \ll 1$.

In Fig. (7), the evolution of the spatially-averaged field and energy components are shown for parameters $\alpha = 10^{-3}$, 10^{-4} and 10^{-5} in descending order. Since the amount of backreaction is dependent on the strength of the field fluctuations, one tell-tale way of identifying it would be to look for the point in time where the gradient energy becomes comparable to the kinetic and potential energies. In other words, $(\tilde{\nabla}\tilde{\phi})^2 \sim \dot{\tilde{\phi}}^2, \tilde{V}(\tilde{\phi})$. From the top panel in Fig. (7), we see that E_G always provides a negligible contribution to the total energy. As a result, there is no noticeable backreaction and the field keeps oscillating with decreasing amplitude. On the other hand, in the middle and bottom panels, we see E_G approaching $\mathcal{O}(E_K)$ and $\mathcal{O}(E_V)$ which, consequently, appears as a backreaction on the evolution of $\tilde{\phi}$. This can be seen in the loss of the oscillatory nature of the field at around $t = 100m^{-1}$, from which point ϕ maintains a steady decay. Although it may not be feasible to exactly pin down the value of α for which backreaction can not be neglected, we find that by narrowing down the range between 5×10^{-4} and 10^{-4} , it is possible to infer when the backreaction starts becoming prominent. For this, we refer to Fig. (8) where the spatially-averaged fields for $\alpha = 2.5 \times 10^{-4}$ and 2×10^{-4} are plotted. Although we observe that oscillatory nature of both parameters get suppressed beyond $t = 100m^{-1}$, it is for $\alpha < 2 \times 10^{-4}$ that this effect starts becoming prominent. Hence, the inflaton evolution can be described as a progression of the following stages (for relevant values of α)

1. Oscillations – During this period the inflaton maintains its coherent oscillatory nature, and hence the inhomogeneities, being negligible, have not started affecting the dynamics.
2. Transition – This is a relatively brief period during which the enhanced field fluctuations begin to backreact on the oscillating inflaton condensate, although not strong enough to completely quench the oscillations. It is during this period that the gradient energy E_G starts growing appreciably towards $\mathcal{O}(E_K)$ and $\mathcal{O}(E_V)$.
3. Backreaction – This is the stage where the enhanced field fluctuations backreact onto the background evolution efficiently, thereby significantly changing its dynamics. As

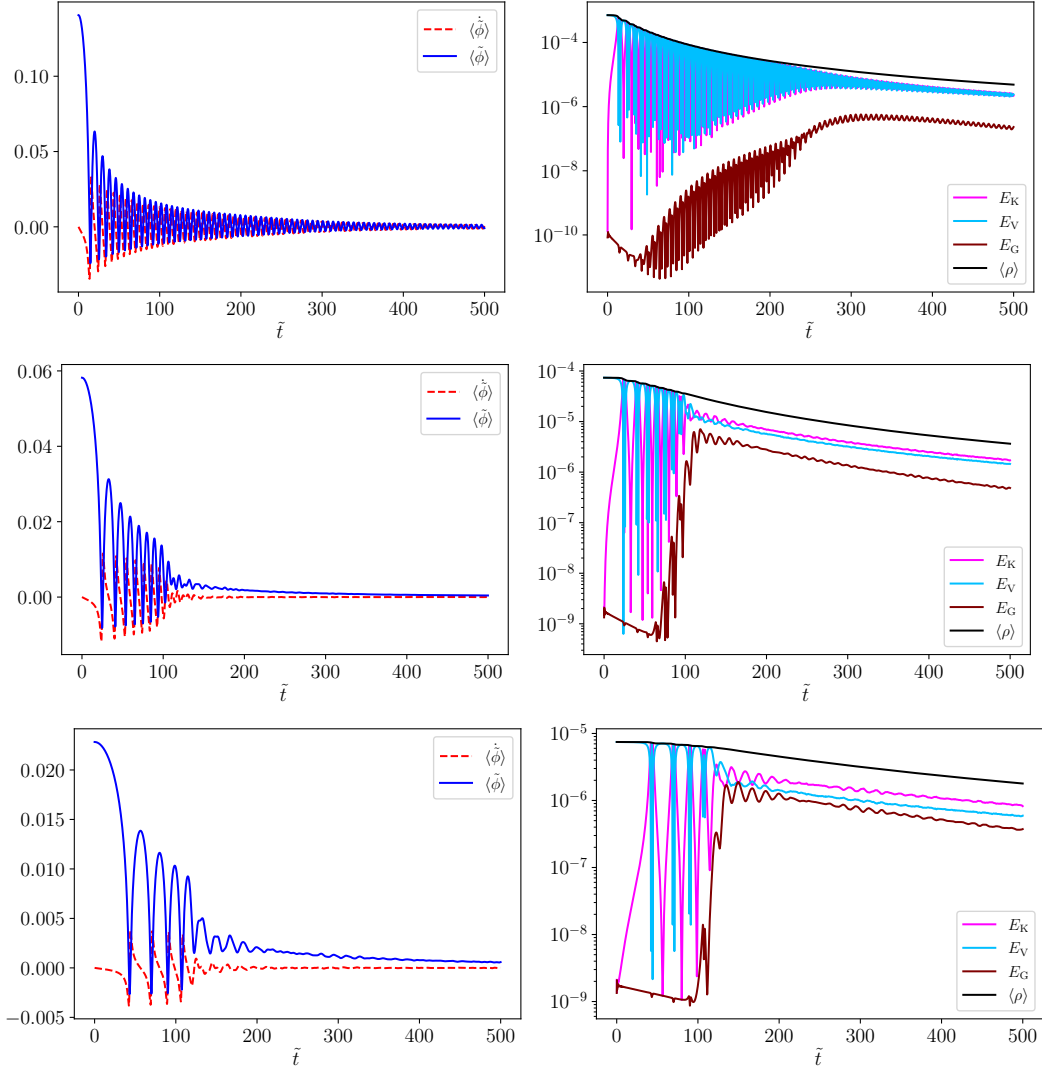


FIG. 7. The evolution of volume averaged fields and energies for $\alpha = 10^{-3}$ (top), 10^{-4} (middle) and 10^{-5} (bottom) respectively. The plots show how, with decrease in α , the $\tilde{\phi}$ field goes from being oscillatory to a loss of oscillatory nature within $t = 100m^{-1}$, suggesting efficient backreaction.

such, the inflaton evolution is no longer oscillatory. Moreover, The backreaction also shuts off the enhancement of the field fluctuations, eventually leading to a truncation in the growth of E_G .

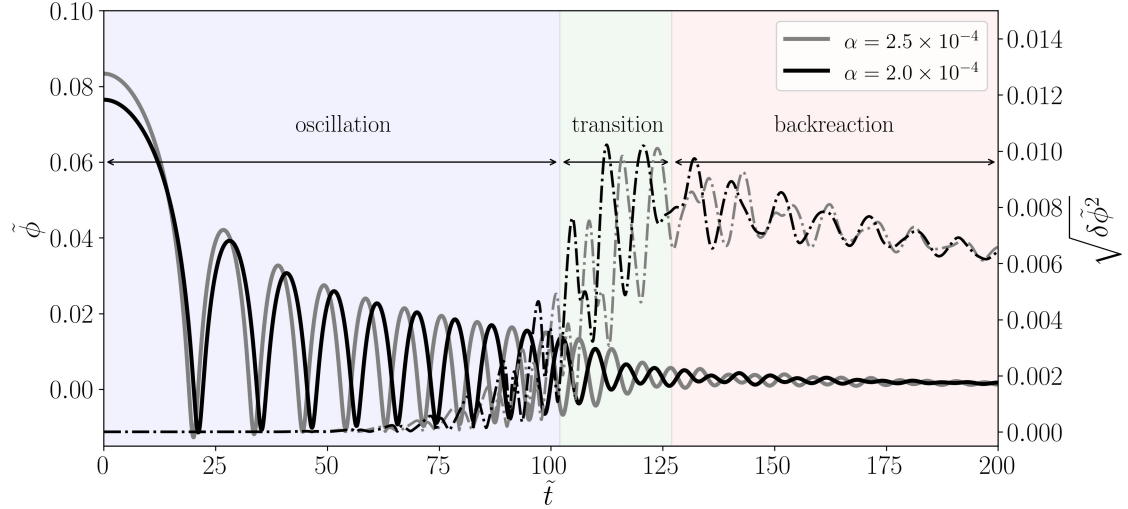


FIG. 8. This figure demonstrates that backreaction effects become prominent for $\alpha \leq 2 \times 10^{-4}$. The solid lines and dash-dotted lines represent $\tilde{\phi}$ and $\sqrt{\delta\tilde{\phi}^2}$ respectively. The evolution of the field can be roughly divided into three parts – (i) oscillations, (ii) transition and (iii) backreaction where we observe during the transition period the size of fluctuations becomes of the order of the field value.

C. Power spectra and nonlinear structure formation

We now consider the growth of perturbations, comparing the lattice data for the power spectrum of inflaton fluctuations $\mathcal{P}_{\delta\phi}(k)$ with our expectations from the linear analysis presented in Sec. III. In Fig. (9), the power spectra for the field fluctuations are shown for parameters $\alpha = 10^{-4}$ (left panel) and 10^{-5} (right panel) with the colorbar indicating the passage of time from $t = 0$ to $500m^{-1}$. The solid black lines represent the power spectrum at $t = 0$. In the figures we see that the smaller modes ($k \lesssim 0.5m$) are the first to get excited since, according to the Floquet charts, these correspond to the physical k -modes which enter the broad resonance band first. Subsequently, the peaks become broader, being shifted towards larger k -modes since these are the ones that enter the broad resonance regime at later times – after the low k -modes have already passed through.

Next we study the spatial configurations of inhomogeneities. *CosmoLattice* is able to generate $3d$ data for the energies E_K , E_V and E_G in HDF5 files which can be used to calculate the spatial distribution of nonlinear structures by computing the density contrast

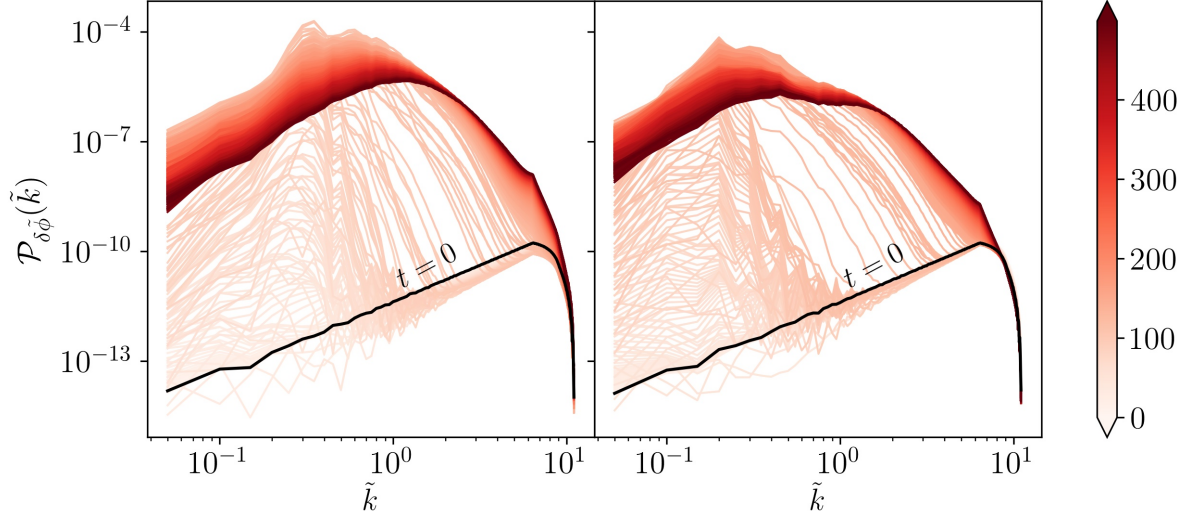


FIG. 9. Power spectra of field fluctuations for $\alpha = 10^{-4}$ (left panel) and $\alpha = 10^{-5}$ (right panel) are shown in the figure with the colorbar representing the progression of time. The solid black lines correspond to the initial power spectra. In these plots $\tilde{k} = k/am$.

$\frac{\delta\rho}{\bar{\rho}}$.⁸ In particular, we refer to Figs. (10) and (11) for $\alpha = 10^{-4}$ and 10^{-5} respectively. The plots are arranged as follows

- The three rows of the figures are density contrast snapshots at three different times – namely $t = 150m^{-1}$, $450m^{-1}$ and $950m^{-1}$.
- In each row, there are two columns. The left column shows a $2d$ contour plot for $\frac{\delta\rho}{\bar{\rho}}$ at a fixed time with an appropriate colorbar. On the other hand, the right column shows a $3d$ isosurface plot for regions where the overdensities exceed 5 times the mean energy density, *i.e.*, $\delta\rho = 5\bar{\rho}$.

We observe, through the $2d$ and $3d$ plots of the overdensities, the existence of highly nonlinear structures that form through the instabilities and subsequent growth of the scalar field perturbations. We note that the grid lengths here do not correspond to the actual comoving lengths of the system but the 256 grid points in each N_x , N_y and N_z . Moving from $t = 150m^{-1}$ to $t = 950m^{-1}$, it is seen that these structures shrink. Since the $3d$ lattices are in comoving units, the shrinking is consistent with the formation of

⁸ The matter of what level of nonlinearity one should look for is rather arbitrary and different authors have used different thresholds in their works (for example, in Ref. [37], the authors chose this threshold to be $\delta\rho = \bar{\rho}$). In this work, we will specifically look for regions in the lattice where these fluctuations are 5 times the mean energy-density.

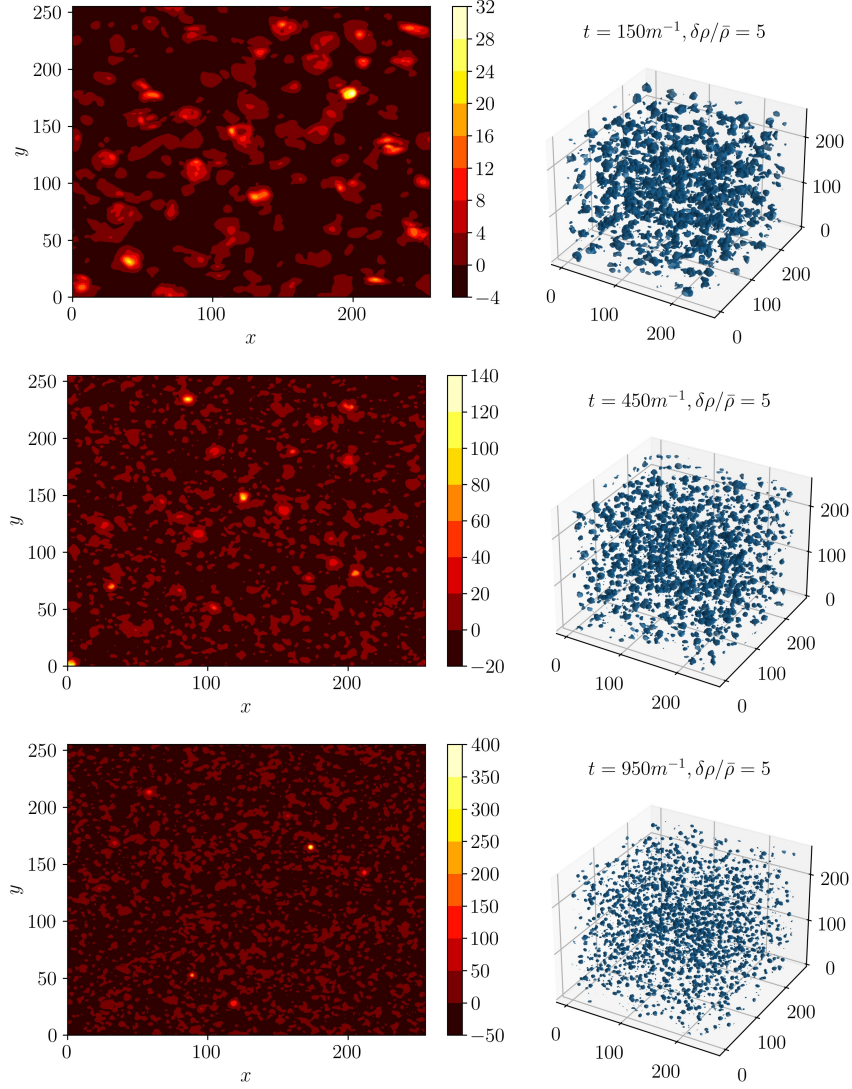


FIG. 10. The density contrast $\frac{\delta\rho}{\bar{\rho}}$ across a $2d$ slice (left panel) and the $3d$ energy isosurfaces for $\frac{\delta\rho}{\bar{\rho}} = 5$ (right panel) are shown here for $\alpha = 10^{-4}$ with $N = 256^3$ grid points. The top, middle and bottom panels represent $t = 150m^{-1}$, $450m^{-1}$ and $950m^{-1}$ respectively. The colorbars next to the $2d$ slices represent the density contrast magnitude and boxes have physical size $L = 125.6m^{-1}$. The sides of these grids and boxes are in comoving lengths with the spatially shrinking overdensities representing oscillons of fixed physical size.

overdensities of constant physical size (see Appendix B). With the passage of time, most of these density fluctuations (or *hot spots*) in the $2d$ slices average around 10 times the mean density with a few isolated peaks. Qualitatively, we also observe differences in the nonlinearities in $\alpha = 10^{-4}$ and 10^{-5} where, in the latter, such regions start out in

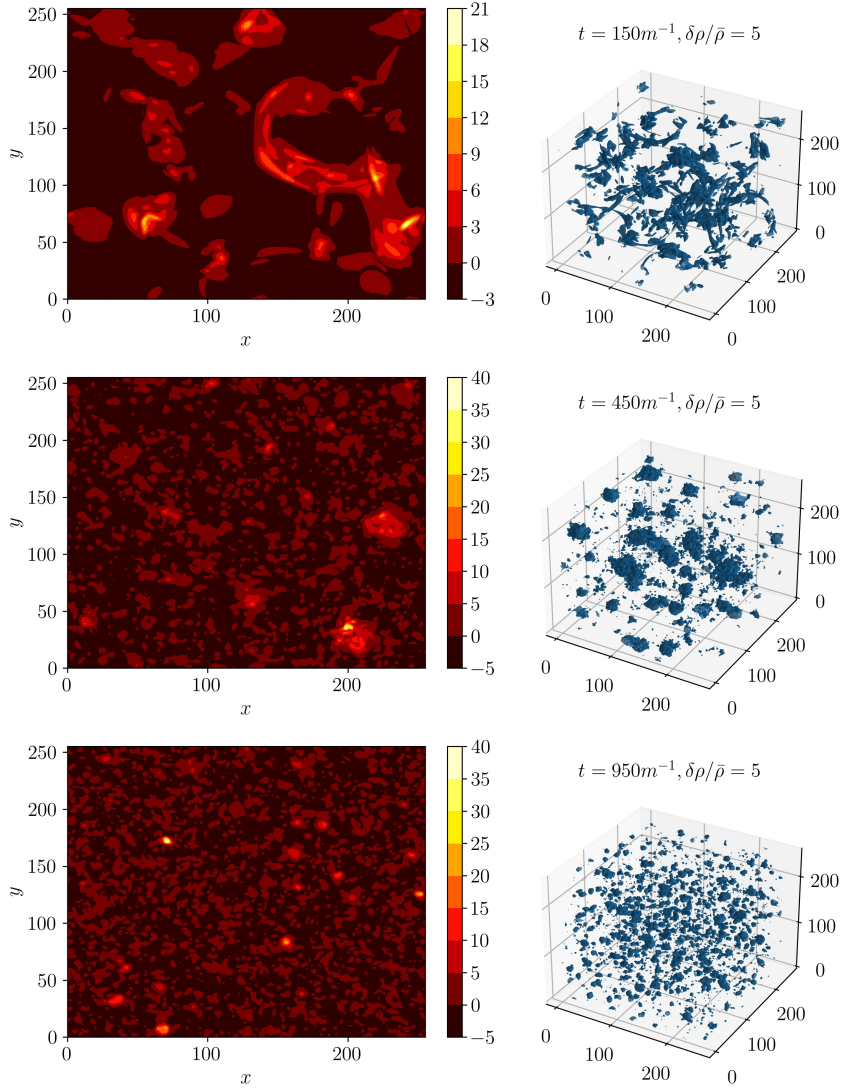


FIG. 11. The density contrast $\frac{\delta\rho}{\bar{\rho}}$ across a $2d$ slice (left panel) and the $3d$ energy isosurfaces for $\frac{\delta\rho}{\bar{\rho}} = 5$ (right panel) are shown here for $\alpha = 10^{-5}$ with $N = 256^3$ grid points. The top, middle and bottom panels represent $t = 150m^{-1}$, $450m^{-1}$ and $950m^{-1}$ respectively. The colorbars next to the $2d$ slices represent the density contrast magnitude and boxes have physical size $L = 125.6m^{-1}$. The sides of these grids and boxes are in comoving lengths with the spatially shrinking overdensities representing oscillons of fixed physical size.

elongated configurations before fragmenting into separate lumps. However, whether or not these nonlinear structures can be considered as oscillons is a matter that needs to be investigated further. This can be studied by observing the long-term behavior of the EoS and whether or not $w \rightarrow 0$, in which case the nonlinear structures can be interpreted as

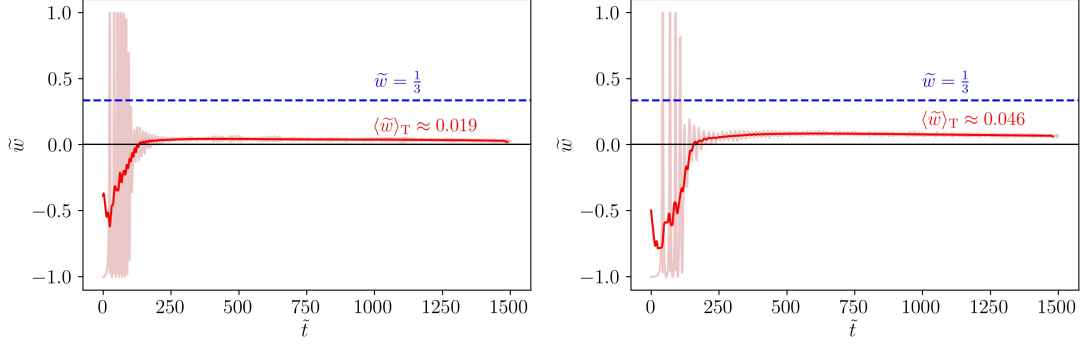


FIG. 12. The plots show the evolution of the spatially-averaged EoS \tilde{w} for $\alpha = 10^{-4}$ (left panel) and $\alpha = 10^{-5}$ (right panel). The solid red lines are obtained by performing a moving average of \tilde{w} , over a suitably defined window, that we define as a time-average $\langle \tilde{w} \rangle_T$. The results of these plots have been generated for $N = 128^3$.

oscillons. We recall that the spatially-averaged EoS is defined as

$$\tilde{w} = \frac{\tilde{P}}{\tilde{\rho}} = \frac{\dot{\tilde{\phi}}^2/2 - (\tilde{\nabla}\tilde{\phi})^2/6a^2 - \tilde{V}}{\dot{\tilde{\phi}}^2/2 + (\tilde{\nabla}\tilde{\phi})^2/2a^2 + \tilde{V}} \quad (\text{IV.7})$$

Furthermore, since the EoS rapidly oscillates compared to the Hubble scale, we also perform a time-average (a moving-average) which we denote by $\langle \tilde{w}_T \rangle$. Using the virial theorem, we can show that the time and spatially-averaged EoS behaves as follows [55]

$$\langle \tilde{w} \rangle_T = \frac{1}{3} + \frac{2}{3} \frac{(n-2)}{(n+1) + \frac{\langle (\tilde{\nabla}\tilde{\phi})^2/a^2 \rangle_T}{\langle \tilde{V} \rangle_T}} \quad (\text{IV.8})$$

for potentials which are $V \propto \phi^{2n}$ near their minima which, in the absence of inhomogeneities, yields the famous result $\langle \tilde{w} \rangle_T = (n-1)/(n+1)$ (see Ref. [81]). However, numerical simulations indicate that for all $n > 1$, contrary to the homogeneous case, the average EoS turns out to be $\langle \tilde{w} \rangle_T \rightarrow 1/3$. In any case, the inflaton fluctuations do not behave like pressureless matter for $n > 1$. If the gradient energy always plays a significantly subdominant role such that $E_G \ll E_V$, then $\langle \tilde{w} \rangle_T \simeq 0$ for $n = 1$, indicating a matter-dominated stage. For the $n = 1$ case of the E-model, the leading order behavior of the potential is quadratic, hence we expect the average EoS to be close to zero at early times when the backreaction effects are negligible.

We expect small deviations from $\langle \tilde{w} \rangle_T = 0$ at intermediate times because of a non-vanishing contribution arising from the gradient energy. Observing the plots on the right

panel of Fig. (7), it is evident that E_G is not completely negligible compared to E_V . As a result, for such intermediate times, we expect the average EoS to be very small, but nonzero nonetheless. However, since E_G falls off faster than E_V with time, the average EoS is expected to asymptotically approach that of pressureless matter. In Fig. (12), the average EoS are plotted for the two α parameters. In the plots, the transparent red curves represent only the spatially-averaged EoS \tilde{w} while the solid red ones include a further time average. It is clear that the nonlinearities that form from preheating behave as pressureless matter which, nevertheless, contains a non-negligible fraction that can constitute of components other than matter. This is evident from the fact that $\langle \tilde{w} \rangle_T$, within the provided range, has a small positive value. Moreover, the average EoS for $\alpha = 10^{-5}$ is slightly larger in this range and can be understood from how the gradient energy behaves for this parameter. Regardless of this, there is evidence that $\langle \tilde{w} \rangle_T$ should approach zero if a longer-term time evolution is considered since the E_G curve diverges away from the one for E_V . These nonlinearities can be regarded as oscillons characterized by a spherically symmetric profile $\phi_{\text{osc}}(t, r)$ peaked at the center and monotonically decaying to zero away from the center. Such profiles should be similar to the secant-type oscillon profiles derived using the small amplitude analysis in Sec. II.

Finally, we can estimate the fraction of the energy density f_{osc} locked in oscillons. A simple prescription for calculating it is given by [49]

$$f_{\text{osc}} \equiv \frac{E_{\text{osc}}}{E_{\text{tot}}} = \frac{\int_{\delta\rho \gtrsim 2\bar{\rho}} d^3\mathbf{x} \rho(\mathbf{x}, t)}{\int d^3\mathbf{x} \rho(\mathbf{x}, t)} \quad (\text{IV.9})$$

where, in the numerator, the 3d energy distribution is integrated for points where the density contrast exceeds two. Since the 3d data are over a 256^3 grid, a straightforward volume integral can prove to be computationally taxing. However, the integrals can be solved very efficiently using a straightforward Monte Carlo integration implementation. With Monte Carlo integration, the integrand

$$I = \int d^3\mathbf{x} \rho(\mathbf{x}, t) \quad (\text{IV.10})$$

can be converted to

$$I \approx \mathcal{V} \frac{1}{N} \sum_{i=1}^N \rho(\mathbf{x}_i, t) \quad (\text{IV.11})$$

where \mathcal{V} is the volume of the lattice and the sum is over a uniform sampling of points in the lattice. Evaluating the integrals for the two parameters, we summarize the results for f_{osc} in Fig. (13). They indeed demonstrate that there is very little nonlinear structure formation before the onset of backreaction, at which point f_{osc} abruptly shoots up to 60%.

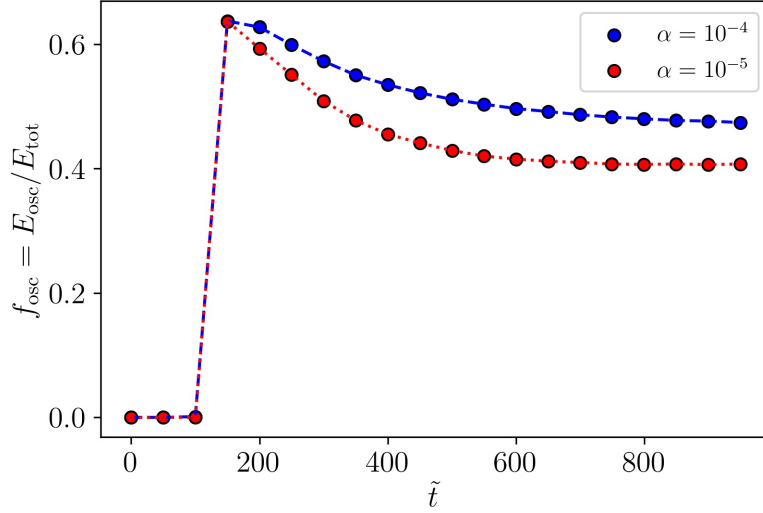


FIG. 13. The fraction of energy contained in oscillons f_{osc} is shown as a function of time. The fraction attains a non-negligible value from the onset of backreaction, then decays to a constant value which it maintains.

After this initial rise, the fraction decays to a constant value such that $f_{\text{osc}} \gtrsim 40\%$ for both parameters. The difference between the values of f_{osc} can be explained by the choice of the threshold for the density contrast since the way the overdensities cluster may be different in the two parameters. Moreover, we can study the $2d$ overdensity plots for another possible answer. In Fig. (10) and (11), we observe that, although the hotspots are similar in distribution, the ones for $\alpha = 10^{-4}$ feature more prominent peaks at certain locations compared to $\alpha = 10^{-5}$. Although not conclusive why there should be different oscillon fractions arising from these two parameters, these provide two possible explanations upon examination of the results. Furthermore, it is possible that the increased abundance of oscillons observed in Fig. (13), as the efficiency of oscillon production is lowered due to backreaction effects, might be related to the inadequate UV resolution of our simulations. This is also indicated by the fact that there is a kink-like feature at late times (around $\tilde{k} \simeq 6$) in the power-spectra of field fluctuations, as can be seen in Fig. (9). We are keen on carrying out a detailed investigation into these issues in a future project.

V. DISCUSSION

We have shown that oscillons can form during the preheating stage of an asymmetric inflationary potential like the α -attractor E-model. In particular, we have demonstrated

that backreaction of field fluctuations onto the homogeneous field evolution becomes significant for $\alpha \lesssim 2 \times 10^{-4}$ leading to the formation of highly inhomogeneous field configurations composed of a significant fraction of long-lived oscillons. This does not imply that oscillons (and other nonlinearities) cannot form for larger values of α and, in fact, they can. However, the fractional energy density of the oscillons will be sub-dominant and the preheating dynamics will be dominated by the coherently oscillating inflaton condensate, given the fact that backreaction effects do not kick in for larger values of α . In this such a scenario we can leverage long-term gravitational effects. Using the linearly perturbed Einstein equations, we can show that the Bardeen potential is given by

$$\Psi_{\mathbf{k}} = \frac{3}{2} \left(\frac{aH}{k} \right)^2 \delta_{\mathbf{k}} \quad (\text{V.1})$$

where $\delta_{\mathbf{k}}$ is the Fourier transform of the density contrast. Typically for $\delta_{\mathbf{k}} \ll 1$ and $k \gg aH$, $\Psi_{\mathbf{k}} \approx 0$ at early times. Nevertheless, one can still expect the formation of nonlinear structure at late times due to the gravitational amplification of metric fluctuations. As briefly mentioned before, the presence of metric perturbations has important consequences for the growth of $\delta\phi_{\mathbf{k}}$, so much so that even for $V(\phi) \sim \phi^2$, for which inflaton self-interaction is absent, Eq. (III.4) takes the form of the Mathieu equation, which is not the case in the absence of metric fluctuations. With this *metric preheating* phenomenon, it has been shown that small scale perturbations are susceptible to parametric resonance which re-enter the horizon during reheating and which are also larger than a characteristic scale given by $\sqrt{3Hm}$ [58, 60, 82]. The effect of gravitational clustering on oscillon formation in this parameter space will be explored in a future work.

It is important to note that the lattice simulation results may change upon further refinement of the lattice size. For the majority of this work, the results reflect the use of $N = 256^3$, $\tilde{k}_{\text{IR}} = 0.05$ and $\tilde{k}_{\text{UV}} = 4$ (ultraviolet cut-off). It is entirely possible that a finer lattice size ($N = 512^3$ or 1024^3) might reveal interesting details about nonlinear structure formation hitherto unseen, although we do not anticipate very large deviations away from the results that have been presented here. As an example, the observation that f_{osc} is less for $\alpha = 10^{-5}$ may have arisen from a lack of resolution in the 3d grids and one may conjecture that refining the grid can reveal finer details and create better parity between the two parameters.

Furthermore, one should also question whether such low values of α perform well with CMB constraints arising from Planck and BICEP/Keck. In the large- N limit, and for $\alpha \leq 1$ the α -attractors exhibit the following universality class for the CMB observables

n_s and r [61, 62]

$$n_s \simeq 1 - \frac{2}{N}, \quad r \simeq \frac{12\alpha}{N^2} \quad (\text{V.2})$$

where $N = N_\star - N_{\text{end}}$ denotes the number of e -folds of expansion in between the Hubble-exit epoch of the CMB pivot scale N_\star and the end of inflation N_{end} . For $\alpha \lesssim \mathcal{O}(1)$ and $N = 55$, the α -attractors provide very robust predictions for such inflationary observables. For example, for $\alpha = 1$ (coinciding with the traditional Starobinsky potential) and $N = 55$, one finds that $n_s \approx 0.964$ and $r \approx 0.004$, which are in excellent agreement with current CMB constraints [7, 8]. However, α -attractors can also produce negligibly small levels of tensor fluctuations depending on the smallness of the value of α , which can have major implications for the running of the scalar spectral index α_s . We recall that the running of the scalar spectral index is defined as

$$\mathcal{P}_\zeta(k) = \underbrace{\mathcal{A}(k_\star)}_{2.1 \times 10^{-9}} \left(\frac{k}{k_\star} \right)^{n_s - 1 + \frac{1}{2}\alpha_s \ln(k/k_\star) + \dots} \quad (\text{V.3})$$

$$\alpha_s \equiv \left. \frac{dn_s}{d \ln k} \right|_{k=k_\star} \quad (\text{V.4})$$

being currently constrained to $\alpha_s = -0.006 \pm 0.013$. In Ref. [83] it was shown that inflationary models described by the first two slow-roll parameters are now excluded with the latest BICEP3/Keck [78, 84] bounds on r . With the latest data, the analysis found a posterior distribution $\mathcal{P}(N)$ preferring $N \gtrsim 80$ with the two-term slow-roll hierarchy. The situation can be ameliorated by considering the first three slow-roll parameters. However, with this, very low values of r in asymptotically flat potentials result in a relatively large running of the scalar spectral index, but are still within current observational bounds on α_s .

VI. CONCLUSIONS

In this paper, we investigated whether oscillons can form in an asymmetric inflationary potential – a question which has not been adequately addressed in the existing literature. We used the α -attractor E-model as a representative asymmetric potential. Using a 4th-order Taylor expansion of the E-model potential, we analytically demonstrated the existence of oscillon-like solutions with a secant-type core. However, the existence of such oscillon-like solutions is not a sufficient condition for oscillon formation and, considering the fact that the 4th-order expression only really works well for $\alpha \sim \mathcal{O}(1)$, a full $3d$ lattice treatment is necessary to verify the formation of nonlinear objects.

We performed a detailed lattice study during preheating in the E-model for three different values of α where we showed that effects of backreaction become significant for $\alpha \lesssim 2 \times 10^{-4}$. This occurs due to a sharp rise in the field's gradient energy which begins to modify the evolution of the oscillating inflaton condensate significantly. In the relevant parameter space, localised and highly nonlinear structures were seen to be formed which maintain roughly constant physical sizes as the universe expands in time. Moreover, the average EoS reveal that they are in fact close to being matter-like (with some non-negligible fraction of the energy being locked into radiative modes which tends to vanish in the asymptotic future. With these in mind, we conclude that indeed a significant amount of oscillons form in this particular example of an asymmetric potential for $\alpha \lesssim 2 \times 10^{-4}$. In relation to the estimate given by Eq. (IV.6) found in Ref. [80], it is seen that the onset of backreaction occurs for much smaller values of α , although it does manage to exclude a large portion of the parameter space.

We bear in mind, however, that we have restricted ourselves to only studying the scalar field fluctuations and gravitational influences arising from metric perturbations have been ignored. As mentioned in Sec. V, for values of α where self-resonance is not as efficient, one can look forward to long-term gravitational effects on the system and the eventual formation of nonlinearities in larger proportions than those formed solely from self-resonance. Such a study will be performed in a future work using full numerical relativity [85]. Moreover, larger values of α will imply larger values of r which will be more favorable in terms of CMB constraints. This is not to say that a very small value of r poses any serious problems. However, as seen in Ref. [83], very small values of r point towards somewhat larger values of the running of scalar spectral index α_s which can impinge on current CMB constraints. Additionally, we note that oscillons, though long-lived, are meta-stable and they eventually decay on longer time scales. We intend to carry out a thorough analysis of oscillon decay in our upcoming paper, focusing on possible astrophysical and cosmological implications both in the case of the inflaton field and ultra-light scalar dark matter.

VII. ACKNOWLEDGMENTS

SSM is supported by an STFC Consolidated Grant [Grant No. ST/T000732/1]. We thank Daniel Figueroa for email correspondences regarding the use of *CosmoLattice* during the initial phase of this project. For the purpose of open access, the authors have applied a CC BY public copyright license to any Author Accepted Manuscript version

arising.

Data Availability Statement: This work is entirely theoretical and has no associated data. The data files for the lattice simulations (with the exception of the $3d$ configuration files) and other codes can be found in the following GitHub repository: https://github.com/RM503/Oscillon_Emodel.

Appendix A: Deriving CosmoLattice parameters from inflationary observables

Here we use CMB constraints on inflationary observables to derive the parameters and initial homogeneous field configurations for CosmoLattice. With an E-model potential of the form

$$V(\phi) = \frac{3}{4}\alpha m^2 M_{\text{pl}}^2 \left(1 - e^{-\sqrt{\frac{2}{3\alpha}} \frac{\phi}{M_{\text{pl}}}}\right)^2 \quad (\text{A.1})$$

the first slow-roll parameter ϵ_v can be used to determine the field value at the end of inflation, which serves as the initial condition for the simulations. Using the fact that

$$\epsilon_v = \frac{M_{\text{pl}}^2}{2} \left(\frac{\partial_\phi V}{V}\right)^2 \quad (\text{A.2})$$

we solve for $\epsilon_v = 1$ to obtain

$$\frac{\phi_{\text{end}}}{M_{\text{pl}}} = \sqrt{\frac{3\alpha}{2}} \ln \left(1 + \frac{2}{\sqrt{3\alpha}}\right) \quad (\text{A.3})$$

The mass scale m is determined through the CMB normalization at the pivot scale k_\star which requires the field value ϕ_\star for some prescribed number of observable e -folds. In the slow-roll regime, the total number of e -folds is given by

$$N(\phi_\star) = \frac{1}{M_{\text{pl}}^2} \int_{\phi_{\text{end}}}^{\phi_\star} \frac{V}{\partial_\phi V} d\phi \quad (\text{A.4})$$

$$= \frac{1}{4} \left[3\alpha \left(e^{\sqrt{\frac{2}{3\alpha}} x_\star} - e^{\sqrt{\frac{2}{3\alpha}} x_{\text{end}}} \right) - \sqrt{6\alpha} (x_\star - x_{\text{end}}) \right] \quad (\text{A.5})$$

where $x = \frac{\phi}{M_{\text{pl}}}$ and x_{end} is determined using Eq. (A.3). Using 55 e -folds as a reference number for observable e -folds, the value of ϕ_\star can be determined as a function of α . Finally, the value of m can be set using the CMB normalization of the primordial power spectrum at k_\star . In slow-roll

$$\mathcal{P}_{\zeta_\star} \approx \frac{V^3}{12\pi^2 (\partial_\phi V)^2 M_{\text{pl}}^6} \quad (\text{A.6})$$

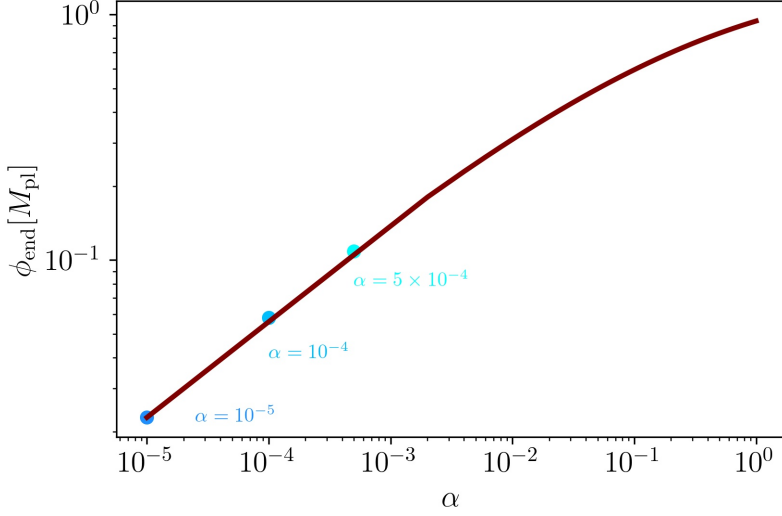


FIG. 14. Variation of ϕ_{end} as a function of α . The three points on the plot indicate the different values of α that were used in the lattice simulations.

such that

$$\frac{m}{M_{\text{pl}}} \approx \sqrt{\frac{128\pi^2 \mathcal{P}_{\zeta_\star}}{3\alpha^2}} \frac{z_\star}{(z_\star - 1)^2} \quad (\text{A.7})$$

where $\mathcal{P}_{\zeta_\star} = 2.1 \times 10^{-9}$ and $z_\star = \exp\left(\sqrt{\frac{2}{3\alpha}} \frac{\phi_\star}{M_{\text{pl}}}\right)$.

Appendix B: Physical sizes of overdensities

In Sec. [IV C](#) we mentioned that the nonlinearities that develop maintain constant physical sizes. This can be demonstrated by using the fact that

$$\tilde{L}_{\text{phys}}(\tilde{t}) = a(\tilde{t})\tilde{L} = \left(\frac{\tilde{t}}{\tilde{t}_0}\right)^{2/3} \tilde{L} \quad (\text{B.1})$$

where the appropriate scale factor for the matter-dominated epoch has been used. In Fig. [\(15\)](#), the $2d$ slices of the overdensities are shown for $\alpha = 10^{-4}$ at four different times where we have zoomed into a 300×300 subset of the overall grid. In the plots, the lengths of the grids have been scaled to reflect the physical sizes of the overdensities and it can be seen that, on average, the nonlinear patches maintain roughly constant physical sizes.

[1] A. A. Starobinsky, JETP Lett. **30**, 682 (1979).

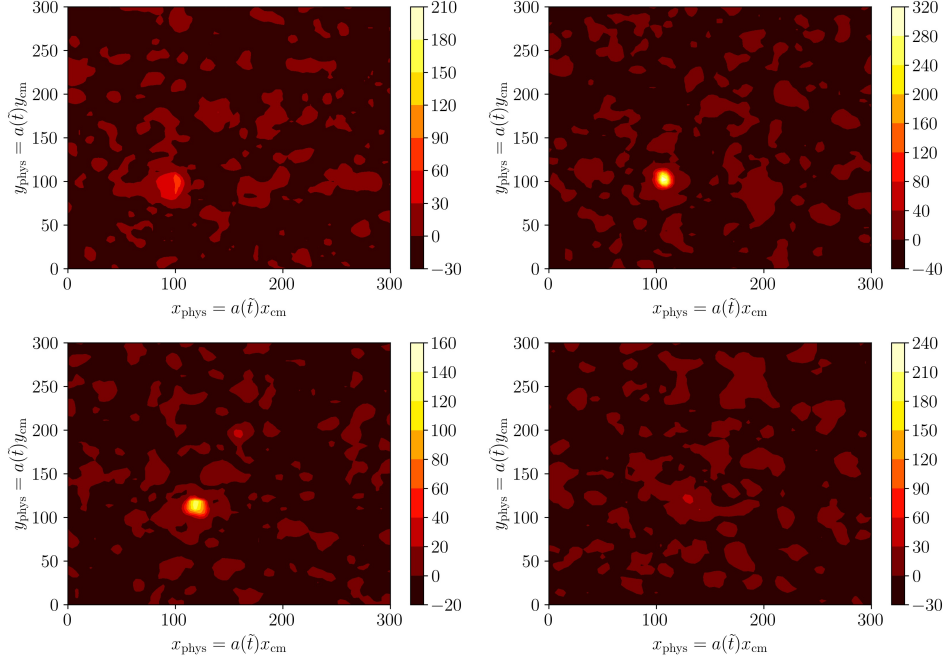


FIG. 15. $2d$ slices of the $3d$ energy isosurfaces are shown here for $\alpha = 10^{-4}$ at different times, where $\tilde{t} = 600$ (top left), 700 (top right), 800 (bottom left) and 900 (bottom right) respectively.

- [2] A. A. Starobinsky, *Phys. Lett. B* **91**, 99 (1980).
- [3] A. H. Guth, *Phys. Rev. D* **23**, 347 (1981).
- [4] V. F. Mukhanov and G. V. Chibisov, *JETP Lett.* **33**, 532 (1981).
- [5] A. H. Guth and S. Y. Pi, *Phys. Rev. Lett.* **49**, 1110 (1982).
- [6] A. D. Linde, *Phys. Lett. B* **108**, 389 (1982).
- [7] N. Aghanim *et al.* (Planck), *Astron. Astrophys.* **641**, A6 (2020), [Erratum: *Astron. Astrophys.* 652, C4 (2021)], [arXiv:1807.06209 \[astro-ph.CO\]](#).
- [8] Y. Akrami *et al.* (Planck), *Astron. Astrophys.* **641**, A10 (2020), [arXiv:1807.06211 \[astro-ph.CO\]](#).
- [9] D. Paoletti, F. Finelli, J. Valiviita, and M. Hazumi, *Phys. Rev. D* **106**, 083528 (2022), [arXiv:2208.10482 \[astro-ph.CO\]](#).
- [10] L. Kofman, A. D. Linde, and A. A. Starobinsky, *Phys. Rev. Lett.* **73**, 3195 (1994), [arXiv:hep-th/9405187](#).
- [11] L. A. Kofman (1996) [arXiv:astro-ph/9605155](#).
- [12] B. A. Bassett, S. Tsujikawa, and D. Wands, *Rev. Mod. Phys.* **78**, 537 (2006), [arXiv:astro-ph/0507632](#).

- [13] R. Allahverdi, R. Brandenberger, F.-Y. Cyr-Racine, and A. Mazumdar, *Ann. Rev. Nucl. Part. Sci.* **60**, 27 (2010), [arXiv:1001.2600 \[hep-th\]](#).
- [14] D. G. Figueroa and F. Torrenti, *JCAP* **02**, 001 (2017), [arXiv:1609.05197 \[astro-ph.CO\]](#).
- [15] M. A. Amin, M. P. Hertzberg, D. I. Kaiser, and J. Karouby, *Int. J. Mod. Phys. D* **24**, 1530003 (2014), [arXiv:1410.3808 \[hep-ph\]](#).
- [16] K. D. Lozanov, (2019), [arXiv:1907.04402 \[astro-ph.CO\]](#).
- [17] I. L. Bogolyubsky and V. G. Makhankov, *JETP Lett.* **24**, 12 (1976).
- [18] M. Gleiser, *Phys. Rev. D* **49**, 2978 (1994), [arXiv:hep-ph/9308279](#).
- [19] A. Kusenko, *Phys. Lett. B* **405**, 108 (1997), [arXiv:hep-ph/9704273](#).
- [20] S. Kasuya, M. Kawasaki, and F. Takahashi, *Phys. Lett. B* **559**, 99 (2003), [arXiv:hep-ph/0209358](#).
- [21] E. Farhi, N. Graham, A. H. Guth, N. Iqbal, R. R. Rosales, and N. Stamatopoulos, *Phys. Rev. D* **77**, 085019 (2008), [arXiv:0712.3034 \[hep-th\]](#).
- [22] E. Clément, L. Vanel, J. Rajchenbach, and J. Duran, *Phys. Rev. E* **53**, 2972 (1996).
- [23] P. B. Umbanhowar, F. Melo, and H. L. Swinney, *Nature* **382**, 793 (1996).
- [24] E. J. Copeland, M. Gleiser, and H. R. Muller, *Phys. Rev. D* **52**, 1920 (1995), [arXiv:hep-ph/9503217](#).
- [25] A. Riotto, *Phys. Lett. B* **365**, 64 (1996), [arXiv:hep-ph/9507201](#).
- [26] N. Graham, *Phys. Rev. Lett.* **98**, 101801 (2007), [Erratum: *Phys.Rev.Lett.* 98, 189904 (2007)], [arXiv:hep-th/0610267](#).
- [27] E. Cotner, A. Kusenko, and V. Takhistov, *Phys. Rev. D* **98**, 083513 (2018), [arXiv:1801.03321 \[astro-ph.CO\]](#).
- [28] E. Cotner, A. Kusenko, M. Sasaki, and V. Takhistov, *JCAP* **10**, 077 (2019), [arXiv:1907.10613 \[astro-ph.CO\]](#).
- [29] J. Y. Widdicombe, T. Helfer, and E. A. Lim, *JCAP* **01**, 027 (2020), [arXiv:1910.01950 \[astro-ph.CO\]](#).
- [30] Z. Nazari, M. Cicoli, K. Clough, and F. Muia, *JCAP* **05**, 027 (2021), [arXiv:2010.05933 \[gr-qc\]](#).
- [31] R. Easther and E. A. Lim, *JCAP* **04**, 010 (2006), [arXiv:astro-ph/0601617](#).
- [32] J. F. Dufaux, A. Bergman, G. N. Felder, L. Kofman, and J.-P. Uzan, *Phys. Rev. D* **76**, 123517 (2007), [arXiv:0707.0875 \[astro-ph\]](#).
- [33] S. Antusch, F. Cefala, and S. Orani, *Phys. Rev. Lett.* **118**, 011303 (2017), [Erratum: *Phys.Rev.Lett.* 120, 219901 (2018)], [arXiv:1607.01314 \[astro-ph.CO\]](#).

- [34] J. Liu, Z.-K. Guo, R.-G. Cai, and G. Shiu, *Phys. Rev. Lett.* **120**, 031301 (2018), [arXiv:1707.09841 \[astro-ph.CO\]](#).
- [35] M. A. Amin, J. Braden, E. J. Copeland, J. T. Giblin, C. Solorio, Z. J. Weiner, and S.-Y. Zhou, *Phys. Rev. D* **98**, 024040 (2018), [arXiv:1803.08047 \[astro-ph.CO\]](#).
- [36] T. Helfer, E. A. Lim, M. A. G. Garcia, and M. A. Amin, *Phys. Rev. D* **99**, 044046 (2019), [arXiv:1802.06733 \[gr-qc\]](#).
- [37] T. Hiramatsu, E. I. Sfakianakis, and M. Yamaguchi, *JHEP* **03**, 021 (2021), [arXiv:2011.12201 \[hep-ph\]](#).
- [38] G. Fodor, P. Forgacs, Z. Horvath, and M. Mezei, *Phys. Rev. D* **79**, 065002 (2009), [arXiv:0812.1919 \[hep-th\]](#).
- [39] M. P. Hertzberg, *Phys. Rev. D* **82**, 045022 (2010), [arXiv:1003.3459 \[hep-th\]](#).
- [40] P. Salmi and M. Hindmarsh, *Phys. Rev. D* **85**, 085033 (2012), [arXiv:1201.1934 \[hep-th\]](#).
- [41] H.-Y. Zhang, M. A. Amin, E. J. Copeland, P. M. Saffin, and K. D. Lozanov, *JCAP* **07**, 055 (2020), [arXiv:2004.01202 \[hep-th\]](#).
- [42] W. Hu, R. Barkana, and A. Gruzinov, *Phys. Rev. Lett.* **85**, 1158 (2000), [arXiv:astro-ph/0003365](#).
- [43] J. Ollé, O. Pujolàs, and F. Rompineve, *JCAP* **02**, 006 (2020), [arXiv:1906.06352 \[hep-ph\]](#).
- [44] M. Kawasaki, W. Nakano, and E. Sonomoto, *JCAP* **01**, 047 (2020), [arXiv:1909.10805 \[astro-ph.CO\]](#).
- [45] E. G. M. Ferreira, *Astron. Astrophys. Rev.* **29**, 7 (2021), [arXiv:2005.03254 \[astro-ph.CO\]](#).
- [46] M. A. Amin, R. Easther, and H. Finkel, *JCAP* **12**, 001 (2010), [arXiv:1009.2505 \[astro-ph.CO\]](#).
- [47] M. A. Amin and D. Shirokoff, *Phys. Rev. D* **81**, 085045 (2010), [arXiv:1002.3380 \[astro-ph.CO\]](#).
- [48] M. A. Amin, (2010), [arXiv:1006.3075 \[astro-ph.CO\]](#).
- [49] M. A. Amin, R. Easther, H. Finkel, R. Flauger, and M. P. Hertzberg, *Phys. Rev. Lett.* **108**, 241302 (2012), [arXiv:1106.3335 \[astro-ph.CO\]](#).
- [50] S.-Y. Zhou, E. J. Copeland, R. Easther, H. Finkel, Z.-G. Mou, and P. M. Saffin, *JHEP* **10**, 026 (2013), [arXiv:1304.6094 \[astro-ph.CO\]](#).
- [51] K. D. Lozanov and M. A. Amin, *Phys. Rev. D* **90**, 083528 (2014), [arXiv:1408.1811 \[hep-ph\]](#).
- [52] Y. Sang and Q.-G. Huang, *Phys. Rev. D* **100**, 063516 (2019), [arXiv:1905.00371 \[astro-ph.CO\]](#).
- [53] S. Antusch, F. Cefala, and S. Orani, *JCAP* **03**, 032 (2018), [arXiv:1712.03231 \[astro-ph.CO\]](#).
- [54] S. Antusch, F. Cefalà, and F. Torrentí, *JCAP* **10**, 002 (2019), [arXiv:1907.00611 \[hep-ph\]](#).

- [55] K. D. Lozanov and M. A. Amin, *Phys. Rev. D* **97**, 023533 (2018), [arXiv:1710.06851 \[astro-ph.CO\]](#).
- [56] K. D. Lozanov and M. A. Amin, *Phys. Rev. D* **99**, 123504 (2019), [arXiv:1902.06736 \[astro-ph.CO\]](#).
- [57] M. C. Johnson and M. Kamionkowski, *Phys. Rev. D* **78**, 063010 (2008), [arXiv:0805.1748 \[astro-ph\]](#).
- [58] K. Jedamzik, M. Lemoine, and J. Martin, *JCAP* **09**, 034 (2010), [arXiv:1002.3039 \[astro-ph.CO\]](#).
- [59] S. S. Mishra, V. Sahni, and Y. Shtanov, *JCAP* **06**, 045 (2017), [arXiv:1703.03295 \[gr-qc\]](#).
- [60] J. Martin, T. Papanikolaou, L. Pinol, and V. Vennin, *JCAP* **05**, 003 (2020), [arXiv:2002.01820 \[astro-ph.CO\]](#).
- [61] R. Kallosh and A. Linde, *JCAP* **07**, 002 (2013), [arXiv:1306.5220 \[hep-th\]](#).
- [62] R. Kallosh, A. Linde, and D. Roest, *JHEP* **11**, 198 (2013), [arXiv:1311.0472 \[hep-th\]](#).
- [63] G. Fodor, P. Forgacs, Z. Horvath, and A. Lukacs, *Phys. Rev. D* **78**, 025003 (2008), [arXiv:0802.3525 \[hep-th\]](#).
- [64] G. Fodor, P. Forgacs, Z. Horvath, and M. Mezei, *JHEP* **08**, 106 (2009), [arXiv:0906.4160 \[hep-th\]](#).
- [65] G. Fodor, *A review on radiation of oscillons and oscillatons*, Ph.D. thesis, Wigner RCP, Budapest (2019), [arXiv:1911.03340 \[hep-th\]](#).
- [66] N. W. McLachlan, *Theory and Application of Mathieu Functions* (Clarendon Press, 1947).
- [67] M. Abramowitz and I. A. Stegun, *Handbook of Mathematical Functions with Formulas, Graphs, and Mathematical Tables* (Dover, New York City, 1964).
- [68] F. Olver, D. Lozier, R. Boisvert, and C. Clark, *The NIST Handbook of Mathematical Functions* (Cambridge University Press, New York, NY, 2010).
- [69] G. N. Felder, J. Garcia-Bellido, P. B. Greene, L. Kofman, A. D. Linde, and I. Tkachev, *Phys. Rev. Lett.* **87**, 011601 (2001), [arXiv:hep-ph/0012142](#).
- [70] G. N. Felder, L. Kofman, and A. D. Linde, *Phys. Rev. D* **64**, 123517 (2001), [arXiv:hep-th/0106179](#).
- [71] E. Tomberg and H. Veermäe, *JCAP* **12**, 035 (2021), [arXiv:2108.10767 \[astro-ph.CO\]](#).
- [72] G. N. Felder and I. Tkachev, *Comput. Phys. Commun.* **178**, 929 (2008), [arXiv:hep-ph/0011159](#).
- [73] A. V. Frolov, *JCAP* **11**, 009 (2008), [arXiv:0809.4904 \[hep-ph\]](#).
- [74] Z. Huang, *Phys. Rev. D* **83**, 123509 (2011), [arXiv:1102.0227 \[astro-ph.CO\]](#).
- [75] J. Sainio, *JCAP* **04**, 038 (2012), [arXiv:1201.5029 \[astro-ph.IM\]](#).

- [76] D. G. Figueroa, A. Florio, F. Torrenti, and W. Valkenburg, *JCAP* **04**, 035 (2021), [arXiv:2006.15122 \[astro-ph.CO\]](#).
- [77] D. G. Figueroa, A. Florio, F. Torrenti, and W. Valkenburg, *Comput. Phys. Commun.* **283**, 108586 (2023), [arXiv:2102.01031 \[astro-ph.CO\]](#).
- [78] P. A. R. Ade *et al.* (BICEP/Keck), in *56th Rencontres de Moriond on Cosmology* (2022) [arXiv:2203.16556 \[astro-ph.CO\]](#).
- [79] J. Kim and J. McDonald, *Phys. Rev. D* **95**, 123537 (2017), [arXiv:1702.08777 \[astro-ph.CO\]](#).
- [80] J. Kim and J. McDonald, *Phys. Rev. D* **105**, 063508 (2022), [arXiv:2111.12474 \[astro-ph.CO\]](#).
- [81] M. S. Turner, *Phys. Rev. D* **28**, 1243 (1983).
- [82] R. Easther, R. Flauger, and J. B. Gilmore, *JCAP* **04**, 027 (2011), [arXiv:1003.3011 \[astro-ph.CO\]](#).
- [83] R. Easther, B. Bahr-Kalus, and D. Parkinson, *Phys. Rev. D* **106**, L061301 (2022), [arXiv:2112.10922 \[astro-ph.CO\]](#).
- [84] P. A. R. Ade *et al.*, *Astrophys. J.* **927**, 77 (2022), [arXiv:2110.00482 \[astro-ph.IM\]](#).
- [85] X.-X. Kou, C. Tian, and S.-Y. Zhou, *Class. Quant. Grav.* **38**, 045005 (2021), [arXiv:1912.09658 \[gr-qc\]](#).